Title
THE ELECTRONIC STRUCTURE OP IV-VI SEMICONDUCTORS

Permalink
https://escholarship.org/uc/item/7h82z3td

Author
Tsang, Yvonne Y.W.

Publication Date
1970

UCRL-19144

THE ELECTRONIC STRUCTURE OF IV-VI SEMICONDUCTORS

Yvonne Y. W. Tsang
(Ph. D. Thesis)

January 1970

AEC Contract No. W-7405-eng-48

LAWRENCE RADIATION LABORATORY
UNIVERSITY of CALIFORNIA BERKELEY

TABLE OF CONTENTS

THE ELECTRONIC STRUCTURE OF IV-VI SEMICONDUCTORS

Yvonne Y. W. Tsang

Inorganic Materials Research Division, Lawrence Radiation Laboratory,
and Department of Physics,
University of California, Berkeley, California

ABSTRACT

The Empricial Pseudopotential Method (EPM) including spin-orbit interaction is applied to SnTe, PbTe and GeTe. The resultant electronic band structures and pseudopotential form factors are used to examine the following:

(1) The imaginary part of the frequency dependent dielectric function is computed in order to analyze the optical properties of all three crystals. (2) The band edge structure near the L point of the Brillouin zone for SnTe, PbTe and (Sn,Pb)Te alloys is studied in great detail. (3) The Fermi surfaces of SnTe and PbTe are mapped out to compare with experiments. (4) A method to calculate the energy shifts arising from changes in temperature is developed within the framework of the EPM and applied to the energy levels at the L point of the Brillouin zone in PbTe. The correct positive sign of the temperature coefficient for the fundamental gap is obtained. (5) The pressure coefficients of the fundamental gap are calculated for SnTe and PbTe. The results are in good agreement with experiment. (6) The pseudopotential form factors are used to calculate the intervalley deformation potential of holes scattered from one pocket near L to another L pocket for SnTe and PbTe. The values obtained are in agreement with values derived from an analysis of the measured superconducting transition temperatures as a function of hole concentration.

I. INTRODUCTION

Using the Empirical Pseudopotenital Method[1] (EPM), we have calculated the electronic band structure of SnTe, PbTe and GeTe (including spin-orbit interactions) to study the electronic properties of these three compounds. The resulting band structures and pseudopotentials were used to examine the optical properties, energy band gap structure, superconducting properties and the temperature dependence of the fundamental energy gap. Many of these properties were first studied experimentally and these measurements provided much of our motivation for the theoretical study.

We will start by reviewing some of the principal experimental results. All three compounds are semiconductors with direct band gaps. PbTe and GeTe can be doped or grown to be both n-type and p-type. SnTe is usually p-type with the holes arising from lack of stoichiometry; i.e. from Sn vacancies. Both GeTe[2,3] and SnTe[4] are superconductors. Work has been done on the visible and ultraviolet optical properties[5] of all three materials to explore the electronic structure at energies higher than the fundamental gap energy. The size of the fundamental band gaps in all three materials are given by tunneling experiments[6] and laser spectroscopy.[7] Shubnikov de-Haas data for PbTe[8] show ellipsoidal Fermi surface around L point of the Brillouin zone; however, the data for SnTe[8a] are complicated and a complete picture of its Fermi surface is still not available.

Some questions have been raised by the experimental results concerning the fundamental energy gap and the electronic structure near the band edge. We list these in turn. First, the temperature dependence of the direct gap in PbTe is considered to be "anomolous", in that the gap gets larger as the temperature is increased. This is contrary to the behavior of the gap in the Group IV semiconductors and in SnTe where the gap decreases as temperature increases. Another interesting question was raised by Dimmock et al.[9] These authors suggested that the ordering of the top valence band and the bottom conduction band energy levels reverses as one goes from SnTe to PbTe. This suggestion was motivated by experiments on alloys of p-type $Pb_{0.81}Sn_{0.19}Te$ at 12°K. The electrons were optically excited by a laser and the emission spectrum gave a direct gap of 0.078eV. The same experimental technique had been applied to p-type PbTe at 12°K[7] and a direct gap of 0.18 eV was observed. Shubnikov de-Haas data gave the fundamental band edge of PbTe at L, Knight-shift experiments[10] and Augmented Plane Wave (APW) band structure calculation[11] found the symmetry of the top valence band to be L_6^+ and that of the bottom conduction band L_6^-. From the tunneling experiment[6] SnTe has a fundamental energy gap of 0.3 eV, the band edge is also expected to be at L from Shubnikov de-Haas data.[8a,12] If the ordering of the top valence band and bottom conduction band were the same in SnTe and PbTe, one should expect the size of the gap in the alloy $Pb_{0.81}Sn_{0.19}Te$ to be between 0.18eV and 0.3eV rather than the small value 0.078 eV that was obtained experimentally, In order to get a consistent picture from the experimental gap data on SnTe, PbTe and the alloy $Pb_xSn_{1-x}Te$, Dimmock et al.[9] proposed the band ordering reversal as one goes from PbTe to SnTe (i.e. the top valence band in SnTe has symmetry L_6^- and the bottom conduction band L_6^+). A previous empirical pseudo-potential calculation was done for SnTe,[13] however, spin-orbit effects were not included and the ordering at the band edge was not determined accurately.

With the rich experimental data available to us, we made a theoretical study of the three compounds, focusing mainly on the questions mentioned in the previous discussion. A pseudopotential band structure calculation including spin-orbit effects for each compound serves as the starting point of our study. Therefore the theory and the band structure calculation for SnTe, PbTe and GeTe is covered in the next chapter (Chapter II). In Chapter III we will discuss the optical constants of these compounds evaluated from the calculated band structures and a comparison with experimental data is made. Chapter IV deals with the band edge ordering and electronic structure near L for PbTe, SnTe and their alloys. The temperature dependence of PbTe energy levels will be discussed in Chapt. V. The case for SnTe is only touched upon briefly. In Chapter VI we present a deformation potential calculation for SnTe and PbTe, this deformation potential is relevant to the superconducting properties in SnTe.

II. THE EMPIRICAL PSEUDOPOTENTIAL METHOD INCLUDING SPIN-ORBIT INTERACTIONS AND ITS APPLICATION TO SnTe, PbTe and GeTe

A. The Pseudopotential Hamiltonian

The use of pseudopotentials for electronic band structure calculations is now common in the study of solids. As an example of the utility of pseudopotentials, the Empirical Pseudopotential Method (EPM) without spin-orbit interaction was used by Cohen and Bergstresser[1] in 1966 to evaluate the band structures of fourteen semiconductors. Since that time the method has been applied with much success to many other materials[13-16]; much of this work and calculations are summarized in the review article by Cohen and Heine.[17] We will therefore review the method briefly and indicate how to incorporate the spin-orbit interaction into this method. The main idea of a pseudopotential is the following: in addition to the usual attractive Coulomb potential, the valence electron sees a repulsive potential arising from the orthogonality of the valence electron wavefunctions to the core electron wavefunctions. The net effect is a weak pseudopotential. We can illustrate the origin of the repulsive term in the following way. In analogy with the OPW method, we write the wavefunction of a valence electron $|\psi_v\rangle$ as a smooth part $|\phi_v\rangle$ minus its projection on all the core states,

$$|\psi_v\rangle = |\phi_v\rangle - \sum_t |b_t\rangle \langle b_t|\phi_v\rangle = (1 - P_c)\, |\phi_v\rangle, \tag{2-1}$$

each core state is denoted by $|b_t\rangle$ and the projection operator on the core state is

$$P_c = \sum_t |b_t\rangle \langle b_t| . \tag{2.2}$$

In band structure calculations, the energy eigenvalues are obtained by solving a secular equation; i.e. to solve for E in the equation:

$$(\mathcal{H} - E)\ |\psi_v\rangle = 0\ , \tag{2-3}$$

we diagonalize the matrix

$$\langle\psi_v|(\mathcal{H} - E)|\psi_v\rangle = 0. \tag{2.4}$$

Substituting Eq. (2-1) into Eq. (2.4), we can write Eq. (2.4) in terms of the smooth part of the valence wavefunction,

$$\langle\phi_v|\ (1 - P_c)\ (\mathcal{H} - E)\ (1 - P_c)\ |\ \phi_v\rangle = 0. \tag{2.5}$$

For the calculation not including spin, the one electron Hamiltonian is

$$\mathcal{H} = p^2/2m + V(r), \tag{2.6}$$

where the first term is the kinetic energy and V(r) is the attractive periodic crystal potential seen by one valence electron. Using Eqs. (2.2), (2.5) and (2.6), we obtain

$$\langle\phi_v|\ [p^2/2m + V(r) + \sum_t (E - E_t)\ |b_t\rangle\ \langle b_t|]\ - E\ |\phi_v\rangle = 0 \tag{2.7}$$

or

$$\langle\phi_v|\ (p^2/2m + V(r) + V_R) - E\ \ |\phi_v\rangle = 0 \tag{2.7a}$$

V_R is the repulsive potential arising from the orthogonality of valence electrons to core electrons, it contains the projection operator and is non local. The sum $V(r) + V_R$ then results in a weak pseudopotential V_p. Therefore, by our definition of $|\psi_v\rangle$ in Eq. (2.1), we have transformed the eigenvalue Eq. (2.4) of the real Hamiltonian $\mathcal{H}$ between actual valence electron wavefunction $|\psi_v\rangle$ to the eigenvalue Eq. (2.7a), where the Hamiltonian is a pseudo-Hamiltonian $\mathcal{H}_p$ and the matrix elements are taken between the pseudo-wavefunctions $|\phi_v\rangle$ (previously called the smooth part of $|\psi_v\rangle$); however, even though we are working with pseudo-wavefunctions and a pseudo-Hamiltonian, we obtain the energy eigenvalues of the actual

Hamiltonian.

For the band calculations, we make the further approximation of assuming a local pseudopotential and expand $V_p(r)$ in the reciprocal space,

$$V_p(r) = \sum_{\underset{\sim}{G}} V(\underset{\sim}{G})\, e^{+i\, \underset{\sim}{G}\cdot r} \qquad (2.8)$$

where $\underset{\sim}{G}$ is a reciprocal lattice vector and

$$V(\underset{\sim}{G}) = \sum_{\alpha} V_\alpha(\underset{\sim}{G})\, S_\alpha(\underset{\sim}{G}), \qquad (2.9)$$

$$S_\alpha(\underset{\sim}{G}) = e^{-i\underset{\sim}{G}\cdot \underset{\sim}{\tau}_\alpha}, \qquad (2.10)$$

$$V_\alpha(\underset{\sim}{G}) = 2/\Omega \int_\Omega V_\alpha(|\underset{\sim}{r}|)\, \ell^{-i\, \underset{\sim}{G}\cdot\underset{\sim}{r}}\, d^3\underset{\sim}{r}. \qquad (2.11)$$

The index α is introduced for crystals with more than one atom per primitive cell, with cell volume Ω, and so $\underset{\sim}{\tau}_\alpha$ is the position of the α^{th} atom with respect to some origin inside a primitive cell. The potential $V_\alpha(G)$ is the Fourier transform of the pseudopotential $V_\alpha(|\underset{\sim}{r}|)$ which is assumed to be spherical about each atom α. We call $S_\alpha(\underset{\sim}{G})$ and $V_\alpha(G)$ the structure factor and the form factor respectively, each corresponding to the α^{th} atom and the reciprocal lattice vector $\underset{\sim}{G}$. Since $|\phi_v\rangle$ is a smooth wavefunction, in our calculation, we expand $|\phi_v\rangle$ in a basis of plane waves $e^{i\underset{\sim}{k}\cdot\underset{\sim}{r}}$ and solve the matrix equation

$$|\mathcal{H}_p^{\underset{\sim}{k}'\underset{\sim}{k}} - E\,\delta_{\underset{\sim}{k}'\underset{\sim}{k}}| = 0 \qquad (2.12)$$

Because the pseudopotential V_p is weak and the pseudo-wavefunction $|\phi_v\rangle$ is smooth, we can truncate the otherwise infinite matrix in solving Eq. (2-12).

We can now put in the spin-orbit term, following essentially Weisz's[18] formulation

$$\mathcal{H}^{s-o} = \hbar/4m^2c^2 \;(\nabla\underset{\sim}{V} \times \underset{\sim}{P}) \qquad (2.13)$$

$$= \underset{\sim}{\Lambda} \cdot \underset{\sim}{\sigma} \,,$$

where V is the periodic crystal potential and σ represents the Pauli spin matrices. Including this term $\mathcal{H}^{s-o}$ in the eigenvalue Eq. (2.5) is equivalent to adding the following term to the pseudo-Hamiltonian

$$\mathcal{H}_p^{s-o} = (1 - P_c)\,\mathcal{H}_{s-o}\,(1 - P_c) \qquad (2.14)$$

in solving the eigenvalue equation

$$\langle\phi_v|\,(p^2/2m + V_p + \mathcal{H}_p^{s-o}) - E\,|\phi_v\rangle = 0 \,. \qquad (2.15)$$

With the inclusion of spin, all our states will now be labeled by a configuration space index as well as a spin index s, therefore, the core states now become

$$|B_R\rangle = |B_{t,s}\rangle \qquad (2.16)$$

and the indices for the basic states of $|\phi_v\rangle$ will be $\underset{\sim}{k}$ for the plane wave and s for the spin. The projection operator becomes,

$$P_c = \sum_R |B_R\rangle\,\langle B_R| = I^{(s)} \sum_t |b_t\rangle\,\langle b_t| \qquad (2.17)$$

where I is the identity in spin space. It is clear then we need the additional matrix element

$$(\mathcal{H}_p^{s-o})_{\underset{\sim}{k}'s',\underset{\sim}{k}s} = (\,(1-P_c)\,\mathcal{H}^{s-o}\,(1-P_c))_{\underset{\sim}{k}'s',\underset{\sim}{k}s} \qquad (2\text{-}18)$$

in solving the secular determinant (2-12) for the band energies. We now write out Eq. (2-18) explicitly:

$$
\begin{aligned}
&\left((1 - P_c)\, \mathcal{H}^{s-o}\, (1 - P_c) \right)_{\underset{\sim}{k}'S',\underset{\sim}{k}S} = \langle \underset{\sim}{k}'s' | \underset{\sim}{\Lambda}\cdot\underset{\sim}{\sigma} | \underset{\sim}{k}s \rangle \\
&- \sum_R \langle \underset{\sim}{k}'s' | B_R \rangle \langle B_R | \underset{\sim}{\Lambda}\cdot\underset{\sim}{\sigma} | \underset{\sim}{k}s \rangle - \sum_R \langle \underset{\sim}{k}'s' | \underset{\sim}{\Lambda}\cdot\underset{\sim}{\sigma} | B_R \rangle \langle B_R | \underset{\sim}{k}s \rangle \\
&+ \sum_{R,R'} \langle \underset{\sim}{k}'s' | B_{R'} \rangle \langle B_{R'} | \underset{\sim}{\Lambda}\cdot\underset{\sim}{\sigma} | B_R \rangle \langle B_R | \underset{\sim}{k}s \rangle \\
&= \langle s' | \underset{\sim}{\sigma} | s \rangle \cdot \{ \langle \underset{\sim}{k}' | \Lambda | \underset{\sim}{k} \rangle - \sum_t \langle \underset{\sim}{k}' | b_t \rangle \langle b_t | \underset{\sim}{\Lambda} | \underset{\sim}{k} \rangle \\
&- \sum_t \langle \underset{\sim}{k}' | \underset{\sim}{\Lambda} | b_t \rangle \langle b_t | \underset{\sim}{k} \rangle + \sum_{t,t'} \langle \underset{\sim}{k}' | b_{t'} \rangle \langle b_{t'} | \underset{\sim}{\Lambda} | b_t \rangle \langle b_t | \underset{\sim}{k} \rangle \\
&= \langle s' | \underset{\sim}{\sigma} | s \rangle \cdot \{ \underset{\sim}{\Lambda}^{p-p} + \underset{\sim}{\Lambda}^{c-p} + \underset{\sim}{\Lambda}^{p-c} + \underset{\sim}{\Lambda}^{c-c} \}. \qquad (2\text{-}19)
\end{aligned}
$$

The four terms in the curly bracket of (2-19) are denoted for obvious reasons by $\underset{\sim}{\Lambda}^{p-p}$, $\underset{\sim}{\Lambda}^{c-p}$, $\underset{\sim}{\Lambda}^{p-c}$ and $\underset{\sim}{\Lambda}^{c-c}$ respectively, the superscript p stands for planewave and superscript c for core. Evaluation of Eq. (2-19) involves solving for terms such as $\langle \underset{\sim}{k} | b_t \rangle$, $\langle \underset{\sim}{k} | \underset{\sim}{\Lambda} | b_t \rangle$ and $\langle b_t | \underset{\sim}{\Lambda} | b_t \rangle$. Appendix A shows the calculation of these matrix elements. It turns out that $\underset{\sim}{\Lambda}^{c-c}$ is several orders larger than the $\underset{\sim}{\Lambda}^{p-c}$ and $\underset{\sim}{\Lambda}^{p-p}$ contributions and we retain only the core-core term, $\underset{\sim}{\Lambda}^{c-c}$.

For the three IV-VI materials which we will consider, the core consists of s, p and d electrons. The s electrons contribute nothing to the spin-orbit interaction, and since the valence electrons SnTe, GeTe and PbTe are s and p-like, we expect the projection of the valence wavefunction onto d core states to be small so that we may also neglect $\langle b_d | \underset{\sim}{\Lambda} | b_d \rangle$ in the core-core term where $| b_d \rangle$ is a d-like core state, we are therefore left with only one contribution in $\underset{\sim}{\Lambda}^{c-c}$ to consider, i.e. the contribution arising from p core electrons. Then Eq. (2-19) becomes:

$$(\mathcal{H}^{p}_{s-o})_{\underset{\sim}{k}'s',\underset{\sim}{k}s} = \underset{\sim}{\sigma}_{s's} \cdot (\hat{k}'\times \hat{k}) \times \sum_{\alpha} -i\, S_{\alpha}(\underset{\sim}{k}-\underset{\sim}{k}')\, \lambda_{\alpha}(k,k') \qquad (2.20)$$

where $S_{\alpha}(\underset{\sim}{k}-\underset{\sim}{k}')$ is the usual structure factor for atom α defined in Eq. (2-10). The angular part of the matrix element $\langle b_p|\underset{\sim}{\Lambda}|b_p\rangle$ gives $-(\hat{k}'\times\hat{k})$ and the radial part gives $\lambda_{\alpha}(k,k')$ which is essentially a product of two orthogonal integrals $B^{*}_{n\ell}(k')$ and $B_{nl}(k)$ multiplied by an adjustable numerical parameter as is shown in Appendix A. The orthogonal integrals are defined in Eq. (A-17) of Appendix A,

$$B_{n\ell}(k') = \int i^{\ell}\,[4\pi(2\ell+1)]^{1/2}\, j_{\ell}(k'r')\, R_{n\ell}(r')\, r'^{2}\, dr' \qquad (2.21)$$

In our case the subscript $\ell = 1$ for p core electrons, $n = 3, 4, 4$ and 5 for Ge, Sn, Te and Pb respectively. We used Herman and Skillman's[19] tabulated atomic p orbitals in a numerical integration of (2.21) to obtain the k,k' dependence of $\lambda_{\alpha}(k,k')$ in Eq. (2.20),

Now we may write down the total pseudo-Hamiltonian matrix element in the plane wave representation

$$\mathcal{H}_{\underset{\sim}{k}'s',\underset{\sim}{k}s} = p^{2}/2m\;\; \delta_{\underset{\sim}{k}'\underset{\sim}{k}}\, \delta_{s's} + \sum_{\alpha=1}^{2} S_{\alpha}(\underset{\sim}{k}-\underset{\sim}{k}') \times [V_{\alpha}(|\underset{\sim}{k}'-\underset{\sim}{k}|)\, \delta_{s's} - i\,(\hat{k}'\times\hat{k})\,\lambda_{\alpha}(|\underset{\sim}{k}|,|\underset{\sim}{k}'|)\cdot \underset{\sim}{\delta}_{s's}]. \qquad (2.22)$$

For binary compounds, it is convenient to decompose both the λ_{α}'s of Eq. (2.20) and the form factors $V_{\alpha}(|\underset{\sim}{k}'-\underset{\sim}{k}|)$ of Eq. (2-11) into a symmetric part and an antisymmetric part, that is,

$$\lambda^{S}(|\underset{\sim}{k}|,|\underset{\sim}{k}'|) = \frac{\lambda_{1}(|\underset{\sim}{k}|,|\underset{\sim}{k}'|) + \lambda_{2}(|\underset{\sim}{k}|,|\underset{\sim}{k}'|)}{2}, \qquad (2.23)$$

$$\lambda^{A}(|\underset{\sim}{k}|,|\underset{\sim}{k}'|) = \frac{\lambda_{1}(|\underset{\sim}{k}|,|\underset{\sim}{k}'|) - \lambda_{2}(|\underset{\sim}{k}|,|\underset{\sim}{k}'|)}{2}, \qquad (2.24)$$

then Te will be labeled by 2 and its position within the primitive cell is,

$$\tau_2 = a\,(1/2,\ 1/2,\ 1/2) \tag{2.31}$$

For the fcc structure factor, we can also show that for each $\underset{\sim}{G} = (h,k,\ell)\ 2\pi/a$, h, k, ℓ must all be odd integers or all be even integers, the former gives odd $|\underset{\sim}{G}|^2$ and the latter gives even $|\underset{\sim}{G}|^2$, then

$$e^{-i\,\underset{\sim}{G}\cdot\tau_2} = \begin{cases} +1 \text{ for even } |\underset{\sim}{G}|^2 \\ -1 \text{ for odd } |\underset{\sim}{G}|^2 \end{cases} . \tag{2.32}$$

Therefore,

$$\begin{aligned} S^S(\underset{\sim}{G}) &= (S_1(\underset{\sim}{G}) + S_2\,(\underset{\sim}{G}))/2 \\ &= \begin{cases} +1 \text{ for } |G|^2 \text{ even} \\ 0 \text{ for } |G|^2 \text{ odd} \end{cases} ,\ \text{and} \end{aligned} \tag{2.33}$$

$$\begin{aligned} S^A(\underset{\sim}{G}) &= (S_1(\underset{\sim}{G}) - S_2(\underset{\sim}{G}))/2i \\ &= \begin{cases} -i \text{ for } |\underset{\sim}{G}|^2 \text{ odd} \\ 0 \text{ for } |\underset{\sim}{G}|^2 \text{ even} \end{cases} . \end{aligned} \tag{2.34}$$

Both SnTe and PbTe have fcc crystal structure while GeTe is face centered rhombic; however, the distortion from fcc is small and we have assumed the fcc structure for all three materials, with lattice constants equal to 6.313Å, 5.996Å, 6.454Å for SnTe, GeTe and PbTe respectively.

The potentials are chosen in the following way. For SnTe, we start with the same set of symmetric form factors used in the previous EPM calculation[13] and vary the two antisymmetric form factors to give a few of the principal gaps. The symmetric form factors are then varied slightly in an attempt to get even closer agreement with the experimental splittings. The form factors chosen were:

$$V^S(G^2 = 4) \;\; -.232 \text{ Ry.}, \quad V^S(8) = -.024,$$
$$V^S(12) = .018, \quad V^A(3) = .055 \text{ and } V^A(11) = .023.$$

These are almost identical with the form factors of Lin et al.[13]; the largest variation is 0.004 Ry. in the symmetric potential and 0.02 Ry in the antisymmetric potential. For GeTe, the starting point for the choosing of the form factors was taken as an average of the Sb and As form factors extracted from the symmetric and antisymmetric form factors of InSb[1] and GaAs,[1] with appropriate scaling factors to account for the lattice changes. (The basic assumption here is that only the lattice constant and not the atomic pseudopotential in real space changes from one crystal to another, then the pseudopotential form factor

$$V_\alpha(G) = 2/\Omega \int V_\alpha\,(|\underset{\sim}{r}|)\;\; e^{-i\underset{\sim}{G}\cdot\underset{\sim}{r}}\, d^3\underset{\sim}{r} \tag{2.36}$$

scales to $\Omega = a^3/4$ in the denominator and $G = 2\pi/a$ in the integrand accordingly). After this set was chosen, the form factors were varied slightly to give some of the observed gaps. The GeTe form factors are $V^s(4) = -.245$ Ry., $V^s(8) = -.022$, $V^s(12) = .032$, $V^A(3) = .060$ and $V^A(11) = .017$.

The form factors for PbTe are obtained in a slightly different fashion from those of SnTe and GeTe. As a first attempt, we merely scaled the SnTe form factors to the PbTe lattice as a test to explore the possibility of a band inversion at the L point going from SnTe to PbTe. The ordering in SnTe is L_6^- for the valence band maximum and L_6^+ for the conduction band minimum with a splitting $L_6^+ - L_6^- = 0.33$eV. Tunneling measurements[6] give 0.3eV at 4.2°K for this gap. The result of the scaling is that the L_6^- and L_6^+ levels move within 0.08eV of each other, but the ordering has not yet reversed. If we had started with a slightly smaller

SnTe gap, the inversion would have taken place. The final form factors for PbTe were chosen to give the gap at L to be $L_6^- - L_6^+ = 0.18\text{eV}$.[7] These form factors were only slightly different from the scaled values for SnTe; the changes were -.01 Ry. in $V^S(G^2=4)$ and -0.003 Ry. in $V^S(G^2=8)$. The values for the form factors are: $V^S(4) = -.241$ Ry., $V^S(8) = -.0352$, $V^S(12) = .017$, $V^A(3) = .052$, and $V^A(11) = .021$. This shift from the scaled values is consistent with the difference between the Pb and Sn potentials as calculated by Animalu and Heine.[23] The calculated Pb potential is more negative for small G's than the Sn potential. We conclude, therefore, that the band inversion at L results both from the lattice constant change and from the difference in the Sn and Pb crystal potentials.

The final sets of form factors used for SnTe, PbTe and GeTe are tabulated in Table 1. The resultant band structures of SnTe, GeTe and PbTe are given in Figs. 1, 2 and 3.

C. Discussion of Resultant Band Structures

All three IV-VI compounds have ten valence electrons (two outermost s-electrons and two outermost p-electrons from the fourth column atom and two s-electrons, four p-electrons from the sixth column atom). Because of the inversion symmetry in the fcc structure and time reversal symmetry, all bands are doubly degenerate throughout the Brillouin zone. In Figs. 1, 2 and 3 we show five doubly degenerate valence bands and a few of the conduction bands. All three band structures give the minimum gap near the L point of the Brillouin zone. PbTe has the minimum gap at L, but in both SnTe and GeTe, the extreme are slighly away from L in the hexagonal face of the fcc Brillouin zone in the direction perpendicular to Λ axis. The L point becomes a saddle point; it is a maximum along the Λ direction, but a local minimum in the direction perpendicular to Λ. We will discuss the band structure near L in more detail in Chapter IV. For this chapter we still refer to the direct gap at L as the fundamental gap. The L gap for SnTe and PbTe were given in Section B to be 0.33eV and 0.18eV respectively; for GeTe $L_6^+ - L_6^- = 0.23$eV, which is consistent with the tunneling value of 0.2eV.[6]

Both SnTe and PbTe have a second valence maximum along the Σ axis (although Fig. 2 seems to indicate the same for GeTe, we are guided by a critical point analysis which only gives a saddle point along Σ rather than an absolute maximum for GeTe). There is experimental evidence for the existence of a second valence maximum in these two crystals[8,24-29] and the Σ axis is a possible choice[13] for this maximum. The second band maximum is 0.15 and 0.3eV below the L valence maximum in SnTe and PbTe respectively. In our calculation we implicitly assume zero temperature values for the fundamental gaps for all three crystals. This gap has a negative temperature coefficient for SnTe[30] and a positive temperature coefficient for PbTe.[34] We therefore expect that at room temperature, the L_6^+ maximum will move closer to the second maximum in PbTe than the L_6^- maximum in SnTe will move to its second maximum.

In the next chapter (Chapter III) we discuss the optical properties of SnTe, GeTe and PbTe derived from our band structure calculations.

III. OPTICAL PROPERTIES OF SnTe, GeTe and PbTe

To analyze the visible and ultraviolet optical properties of these crystals, we have computed the imaginary part of the frequency dependent dielectric function $\epsilon_2(\omega)$. The determination of $\epsilon_2(\omega)$ requires a knowledge of the energy bands throughout the Brillouin zone since this function has the form

$$\epsilon_2(\omega) = \frac{e^2 \hbar^2}{3\pi m^2 \omega^2} \sum_{c,v} \int \delta\left(E_c(\underset{\sim}{k}) - E_v(\underset{\sim}{k}) - \omega\right) \times \left| \langle u_{\underset{\sim}{k}v} | \underset{\sim}{\nabla} | u_{\underset{\sim}{k}c} \rangle \right|^2 d^3\underset{\sim}{k} \qquad (3\text{-}1)$$

where $u_{\underset{\sim}{k},v}$ and $u_{\underset{\sim}{k},c}$ are the periodic parts of the valence and conduction band wavefunctions. The interband energies and the dipole matrix element are obtained from eigenvalues and eigenvectors of the pseudo-Hamiltonian. A factor of two arising from spin degeneracy is included in Eq. (3-1) because all bands are doubly degenerate even with spin-orbit effects. Because of the cubic symmetry of SnTe, GeTe and PbTe, band energies and eigenvectors for the dipole matrix element in Eq. (3.1) need only be calculated in 1/48 of the Brillouin zone. The Hamiltonian matrix is diagonalized and the dipole matrix elements computed for a mesh of 356 points in this subzone. Approximately 3×10^6 sampling points are chosen randomly by a Monte Carlo method, the energy eigenvalues and dipole matrix elements associated with each point are obtained by interpolation between the points on the mesh. The resultant $\epsilon_2(\omega)$ for SnTe, GeTe and PbTe are given in Figs. 4, 5, and 6 respectively. Part of these results have been published earler.[32,33] The integration over $\underset{\sim}{k}$ space in Eq. (3.1) may also be written as

$$\int d^3\underset{\sim}{k} = \int \frac{dS}{|\nabla_{\underset{\sim}{k}}\omega|} \qquad (3.2)$$

where S is a surface of constant interband energy $\omega = E_c - E_v$, the prominent optical structure in $\epsilon_2(\omega)$ originates from Van Hove singularities[34-36,17] at the critical points (c.p.) where $\nabla_{\underset{\sim}{k}}\omega = 0$. These critical points can be classified according to symmetry[21] (minima, saddle points and maxima) M_0, M_1, M_2 and M_3. The critical point analysis for SnTe, GeTe and PbTe is given in Tables 2).

For SnTe the onset of our $\epsilon_2(\omega)$ spectrum occurs near 0.3eV coming from transitions near the fundamental band gap at L, this is in good agreement with tunneling data.[6] The drop in intensity at 0.7eV is not attributed to any critical point, but rather to a lack of interband transitions with direct energy differences in this energy range. The spectrum rises again above 0.85eV to give the first peak at 1.1eV as compared to the experimental transmission peak at 0.97eV.[5] This peak comes from a M_0 critical point arising from transitions from band 5 to 6 at the second valence band maximum along Σ. Transition from this ame valence band maximum to band 7 give rise to the main peak at 2.0eV; the decrease above this peak arises from a strong M_2 critical point from transition along Δ. The 3.2eV shoulder observed in the optical reflectivity spectrum is identified as arising from a $4 \rightarrow 7$ band transition along Σ(critical point symmetry M_1 at 3.0eV) and a $4 \rightarrow 6$ band transition along Δ(critical point symmetry M_2 at 3.02eV). The relative intensity of this shoulder is too low compared with optical reflectivity data. We attribute this to the fact that the pseudo-wavefunction dipole matrix elements for the Δ transition here are about two orders smaller than that of the Δ transition responsible for the main peak at 2.0 eV. The three high energy bumps 6. eV, 7.5 eV, 8.7 eV, in the calculated $\epsilon_2(\omega)$ are shifted considerably from their experimental[5] values 6.1 eV, 7.4 eV, and 9.5 eV respectively; they appear to arise mainly from clusters of critical points, i.e. there are a large number of transitions between bands with interband energy in the above range.

The analysis of the GeTe $\epsilon_2(\omega)$ spectrum is very similar to that of SnTe. The onset of the spectrum comes from the fundamental band gap[6] at L at 0.23 eV. The ϵ_2 function then drops slightly because of lack of volume, but it rises quickly after 0.63 eV, as predicted by the onset of the experimental[37] transition spectrum. The main peak occurs at 2.1 eV. The shoulder at 3.3 eV is again low in intensity because of small matrix elements as well as a lack of volume. The two high energy bumps 7.5 eV, 8.25 eV, are shifted from the experimental[5] values 6.2 and 7.8 eV. Again these arise from clusters of critical points.

For PbTe, the onset of the $\epsilon_2(\omega)$ spectrum comes from the fundamental band gap at L near 0.18 eV.[7] Transition from band 5 to 6 at the second valence maximum along Σ gives rise to the M_0 critical point at 1.07 eV the spectrum rises sharply above this point. The main peak at 2 eV again arises from transitions between bands 5 and 7 at Σ and between band 5 and 6 at Δ. This energy is 0.2 eV lower than that given by optical reflectivity data.[5] The shoulder at 3.1 eV is again low in intensity and given by the same transitions as in the case of SnTe and GeTe. The experimental value of this shoulder is 3.36 eV. The two high energy peaks in our ϵ_2 spectrum (6.9 and 7.6 eV) come from a cluster of critical points, mainly near the X points in the zone , and they correspond to the two experimental peaks (6.3 and 7.8 eV) in the optical reflectivity data.[5]

The agreement between the calculated optical spectrum and experiment is better at low energies than at higher energies. This is what one usually expects for the EPM, however, the shifts from experiment at high energies are relatively larger than observed for several other crystals.[38-40] We also note that we are comparing the calculated $\epsilon_2(\omega)$ with reflectivity since an experimental $\epsilon_2(\omega)$ is not available.

IV. ELECTRONIC BAND STRUCTURE AND FERMI SURFACE NEAR THE FUNDAMENTAL ENERGY GAP FOR SnTe and PbTe

In this chapter, we present results from a detailed study of the valence and conduction band structure near the fundamental band gap for PbTe and SnTe. In the critical point analysis of $\epsilon_2(\omega)$ for SnTe, we discovered that the minimum band gap was not at L. If we take a coarse mesh in evaluating $\epsilon_2(\omega)$, we obtained an M_0 critical point for the transition from the top valence band (band 5) to the bottom conduction band (band 6) at L, i.e., this transition has lower interband energy than the two neighboring $\underset{\sim}{k}$ points along the principal axes (these points are $2\pi/a$ (0.429, 0.429, 0.429) and $2\pi/a$ (0.571, 0.5, 0.429) in the mesh of 356 points we have chosen for the $\epsilon_2(\omega)$ calculation). However, a finer mesh shows that for a mesh point not on the principal axes but close to L, i.e. $\underset{\sim}{k} = 2\pi/a$ (0.5, 0.5, 0.429), the interband energy (band 5 → band 6) turned out to be 0.06eV lower than the 0.33eV given by the L point transition.

A. Electronic Structure Near L for SnTe, PbTe and (Sn,Pb)Te Alloys

For PbTe the caluclated gap is at the L point. The valence band symmetry is L_6^+ and the conduction band is L_6^-. The calculated splitting is 0.18eV. In SnTe, the ordering of the bands reverses and the energy surface at L is a saddle point. The valence band energy decreases as one moves away from L along Λ but increases in the direction perpendicular to the Λ axis at L as shown in Fig. 7. The extrema for both the valence and conduction bands lie in the hexagonal face of the Brillouin zone displaced from L by approximately 1/25 of the (1,1,1) reciprocal lattice vector.[33] The hump shape of energy bands in the hexagonal face in SnTe results from ordering of bands at L. If we explore (using a simple perturbation model) what happens as we go from the PbTe band ordering at L to that of SnTe, the bands would cross at the point of the hump structure (Fig. 7) if they did not interact with each other. The bands do, however, repel each other, thus forming gaps at this point. Because of the larger band mass along Λ direction, this hump structure does not appear along this direction. Figure 8 illustrates this in a qualitative way. The magnitude of the gaps at L and near L are sensitive to the pseudopotential. However, the hump shape of the energy bands in the hexagonal face in SnTe is invariant to the choice of potential once the bands have crossed. Band edge structure for alloys of SnTe and PbTe verify this (Fig. 7).

We have computed the band structure of alloys $Sn_X\, Pb_{1-X}Te$ for X = 0.25 0.5, and 0.75. The method of computation is straight forward, the lattice constant, a , was scaled linearly, that is,

$$a(Sn_x\, Pb_{1-x}\, Te) \;=\; x\, a_{SnTe} + (1-x)\, a_{PbTe} \qquad (4.1)$$

the form factors are then scaled to the alloy lattice constant according to Eq. (2.36). The values of lattice constants, form factors and spin-orbit parameters for the alloys as well as for pure SnTe and pure PbTe are tabulated in Tabe 3. The resultant band structures very near L are plotted in Fig. 7 for the directions parallel and perpendicular to the Λ axis. Since we are looking at detailed structure in a small region (about 1/16 of the Brillouin zone), we have used the E_1 = 10 instead of 9 in this calculation in order to keep the size of the Hamiltonian matrix constant throughout the calculation. This eliminates the possibility of spurious effects in the band edge structural arising from the different convergence limits of the matrix sizes. The results shown in Fig. 7 clearly agrees with our prediction Fig. 8.

We might add here that in our critical point analysis for GeTe, we found that at point $\underset{\sim}{k} = 2\pi/a\ (0.5, 0.5, 0.429)$, the conduction band is about .002eV lower than that at L but the valence band maximum still occurs at L so that the interband energy is still a minimum at L. Since GeTe has the SnTe band ordering at L in our EPM calculation, only with a smaller gap (0.2eV), we expect the GeTe energy bands to be similar to those of $Sn_{0.75}Pb_{0.25}Te$ (Fig. 7d) which has the "hump" structure, but much less prominent than in the case of SnTe, which has a larger gap equal to 0.33eV.

B. Fermi Surfaces for PbTe and SnTe

The inversion of the ordering of the bands which makes the L point of the zone not an extremum but a saddle point has interesting effect on the Fermi surface of SnTe. We have mapped out the Fermi surfaces of PbTe and SnTe. In the PbTe case we obtain ellipsoidal surfaces centered at the L point with major axis along L, whereas for SnTe, each pocket of holes centered about L consists of multiply connected surfaces. We will next discuss the method of computation and results in the following paragraphs.

To map out the energy surfaces, we make use of the symmetry of the problem to choose the most efficient set of sampling points in the Brillouin zone near L, i.e., we would like to solve the energy eigenvalue problem on a computer for the smallest number of points possible and still obtaining an adequate picture of the energy contours. We decided to choose a cylindrical co-ordinate system in reciprocal space, with L as the origin and ΓL, the Λ direction, as our z axis. The polar angle θ is then defined in the planes perpendicular to this z axis. We let $\theta = 0$ to be the direction parallel to LW line. The three-fold rotation symmetry about the z axis and the reflection symmetry about the $\theta = 30^\circ$ and $\theta = 90^\circ$ planes allows us to confine our sampling points in the two regions: (i) $0^\circ < \theta < 30^\circ$ and (ii) $60^\circ < \theta < 90^\circ$. Every sampling point is defined by its coordinates (k_t, θ, k_z) where k_t and k_z are the transverse and longitudinal components of the $\underset{\sim}{k}$ vector, expressed in units of $(2\pi/a)$. Sample points are taken with k_t in 0.02 $(2\pi/a)$ intervals and k_z in 0.04 $(2\pi/a)$ intervals, and one (at most two) value of θ in each of regions (i) and (ii) seemed to serve our purpose adequately. The energies of other $\underset{\sim}{k}$ points in the reciprocal space are linearly interpolated from the energies of the grid of the above sampling points.

The valence band energy contours are drawn in planes of constant k_z: $k_z = 0$, $k_z = .04$ $(2\pi/a)$ and $k_z = .08$ $(2\pi/a)$ for SnTe are shown in Figs. 9a, 9b and 9c). We do not show energy contours for PbTe since they are merely circles for each constant k_z plane for an ellipsoidal surface. From these energy contours, we computed, for various Fermi energy levels, the corresponding hole carrier concentration required to fill up to this level. The results are given in Table 4.

The Fermi surface of SnTe consists of four pockets, each centered about an L point of the Brillouin zone. For low concentration (for example, the experimentally attainable 5×10^{19} carriers cm^{-3}), each pocket resembles a "hollowed cylinder", the "mean inner radius" of this "hollowed cylinder" is smallest at L and increases as one moves away from L along the Λ direction. For higher carrier concentrations, the central part of the "cylinder" in the immediate vicinity of L becomes filled with carriers and the cylinder is no longer hollow at this point. For states near the Λ axis further away from L the cylinder remains hollow. This is a characteristic features of the theoretically calculated Fermi surface which persists for all carrier concentrations greater than 7×10^{19} cm^{-3}. In order to get a clearer picture of the actual Fermi surface, we made a cardboard model of one of the energy pockets with an assumed Fermi energy of -0.11 eV (this energy corresponds to the 0.04 eV contour in Fig. 9 since the zero energy reference here is taken to be at the valence maximum which is 0.07eV higher than the energy at L point). This Fermi energy, -0.11eV corresponds to a total carrier concentration of approximately 10^{20} cm^{-3}. The two views of this model in Fig. 10 demonstrates the characteristic features of the calculated Fermi surface which were described earlier. The three-fold symmetry and the multiply-connected nature of the energy pocket which show up in Fig. 10 explains the use of quotation marks around terms such as "radius" and "cylinder" used earlier to describe the surface since these terms implied an analytic surface with a rotational symmetry this surface does not have. As stated earlier, our band structure also gives a second valence band maximum along Σ direction. However, in order for the hole Fermi energy to reach this second valence band maximum, the calculation predicts that a carrier concentration of at least 2.1×10^{20} carriers cm^{-3} must be reached. This is in good agreement with Shubnikov-de Haas experimental data[8a] which indicates that the effect of the presence of holes in a second valence band becomes evident for hole carrier concentrations greater than 2.0×10^{20} carriers cm^{-3}. For lower carrier concentrations between 1.00 to 1.03×10^{20} cm^{-3},[8a] all the carriers can be accounted for in the four pockets of Fermi surface centered about L. The experimental data for SnTe are complicated and the exact shape of these pockets is not yet mapped out experimentally. There have been some suggestions[41] that the "knobs" on our theoretical Fermi surface might lead to extremal areas which can explain some of the experimental results. However, because of the non-analyticity of our calculated Fermi surface, our past attempts to extract extremal areas from it in order to compare with experiments have not been fruitful. It is therefore still an open question as to the extent to which our present theoretical model for the Fermi surface of SnTe corresponds to reality.

The calculated Fermi surface for PbTe are ellipsoids along the [1,1,1] directions centered at L. For carrier concentrations up to 10^{19} cm^{-3}, the anisotropy ratio $K = m^*_\ell / m^*_t$ increases almost linearly with carrier concentration and its value does not exceed two. In particular, for carrier concentrations below 0.3×10^{19} cm^{-3}, the anisotropy ratio becomes slightly less than one so that the ellipsoids are oblate with respect to the [1,1,1] directions. Cyclotron resonance and Shubnikov-de Haas[8] experiments give a much larger anisotropic ratio than the theoretical result. For a carrier concentration of 1.2×10^{18} cm^{-3}, the experiments give K = 9. Therefore, only qualitative agreement at high densities with experiment was obtained from the calculation of Fermi surface for PbTe.

Lastly, we investigated another band edge property: the variation of the energy gap at L for PbTe with changes in the lattice constant. We have related this to the pressure dependence of the direct gap,

$$\left.\frac{\partial E_g}{\partial P}\right|_T = \left.\frac{\partial E_g}{\partial V}\right|_T \left.\frac{\partial V}{\partial P}\right|_T . \qquad (4.2)$$

the value obtained was $\partial E_g / \partial P | T = -7.0\times10^{-6}$ eV/Bar, the experimental value[42] is $(-7.4 \pm 0.2)\times 10^{-6}$ eV/Bar. The calculated value involved the use of the measured compressibility[42] which give $1/V\ \partial V/\partial P|_T = -2.55\times 10^{-6}$ Bar^{-1}. If in PbTe, the ordering ofthe bands at L would have been the same as in SnTe, we would have gotten a positive value for $\partial E_g/\partial P|_T$.

We conclude then that the different band ordering obtained from our EPM calculation for SnTe and PbTe is crucial in explaining qualitatively the experimental Fermi surface results. The ordering is again important in giving good quantitative agreement with experiment for the "anomalous" energy gap temperature dependence $\partial E_g/\partial V|_T\ \partial V/\partial T|_P$ (Chapter V) and the positive sign in the pressure dependence $\partial E_g/\partial P|_T$ in PbTe.

V. EFFECT OF TEMPERATURE ON THE FUNDAMENTAL ENERGY GAP AT L

Experiments[31,42] at constant pressure show the energy gap of PbTe increases linearly with temperature in the temperature range from 80°K to 350°K; for higher temperatures the $E_g(T)$ curve approaches a constant value. The value of the linear temperature coefficient $\partial E_g/\partial T|_P$ lies between 4.1[31] and 4.5×10^{-4} eV/°K.[42] The positive sign of the temperature coefficient is interesting since most common semiconductors (including SnTe) have negative temperature coefficients. PbTe is therefore considered to be "anamolous." In this section, we outline a theoretical calculation of $\partial E_g/\partial T|_P$ using the pseudopotential method for PbTe and compare the results with experiment. We will conclude this section with a detailed discussion of our results.

A. Theory of the Explicit Temperature Dependence of Band Energies

Brooks and Yu[43,44] have shown that the explicit temperature dependence of energy bands in solids may be computed by including the Debye-Waller factor in the structure factor of the potential. We will essentially rederive their result here within the framework of the pseudopotential method which was outlined in the second chapter.

The Born-Oppenheimer[45] approximation allows one to write the Hamiltonian for the electrons in solids as if the electrons were in a static lattice. In the zero temperature band structure calculation in Chapter II we have taken the static lattice to be one where all the cores are at the equilibrium position, then solve for the eigenvalues E_v and the pseudo-wavefunctions $\phi_v(\underset{\sim}{r})$ which are the eigenfunctions of the pseudo-Hamiltonian (Eq. 2.15)

$$(p^2/2m + V_p + \mathcal{H}_p^{s-o})\,\phi_v(\underset{\sim}{r}) = E_v\,\phi_v(\underset{\sim}{r}) = \mathcal{H}_e\,\phi_v(\underset{\sim}{r}) \qquad (5.1)$$

where both E_v and $\phi_v(\underset{\sim}{r})$ correspond to cores assumed to be in equilibrium positions. At finite temperature, the lattice is not frozen so that E_v and $\phi_v(\underset{\sim}{r})$ will be dependent on the instantaneous core configurations. We will denote the configurations by $\{\underset{\sim}{R}_{\ell,\alpha}\}$, the set of core co-ordinates, ℓ indexing the primitive cells and α indexing the basis. Therefore $\phi_v(\underset{\sim}{r})$ and E_v become $\phi(\underset{\sim}{r}, \{R_{\ell,\alpha}\})$ and $E_v(\{R_{\ell,\alpha}\})$ respectively. Since experimental measurements of the electronic energies cannot be carried out instantaneously, the observed electronic energies are actually the time average of the energies $E_v(\{R_{\ell,\alpha}\})$. Assuming the validity of the ergodic theorem, we replace the time average by an ensemble average over all the sets of core wavefunctions. For our calculation, we use the harmonic approximation to simplify the potential energy of the core system, so that the core wavefunctions $\chi_j(\{R_{\ell,\alpha}\})$ may be regarded as the wavefunctions describing the phonon system. Just as in Chapter II we solved for the band energies by diagonalizing a matrix

$$\langle\phi_v(\underset{\sim}{r})\,|\,\mathcal{H}_e - E_v|\,\phi_v(\underset{\sim}{r})\rangle = 0, \qquad (5.2)$$

and now we take the ensemble average of (5.2), that is

$$\langle\chi_j(\{\underset{\sim}{R}_{\ell,\alpha}\})\,|\,(\phi_v, \mathcal{H}_\ell\,\phi_v)\,|\,\chi_j(\{\underset{\sim}{R}_{\ell,\alpha}\})\rangle_{Av} = \langle E_v(\{\underset{\sim}{R}_{\ell,\alpha}\})\rangle_{Av}. \qquad (5.3)$$

The averaging process in Eq. (5.3) gives rise to a temperature dependence of the electronic energies at constant volume.

We proceed first with the pseudopotential term V_p in Eq. (5.3); the core motion is accounted for by writing

$$V_p(\underset{\sim}{r}) = \sum_{\ell\,\alpha} V(\underset{\sim}{r} - \underset{\sim}{R}_{\ell,\alpha}), \qquad (5.4)$$

where

$$\underset{\sim}{R}_{\ell\alpha} = \underset{\sim}{R}^{\circ}_{\ell,\alpha} + \delta\underset{\sim}{R}_{\ell,\alpha} , \tag{5.5}$$

$\underset{\sim}{R}^{\circ}_{\ell,\alpha}$ being the equilibrium position of the ℓ, α core and $\delta\underset{\sim}{R}_{\ell,\alpha}$ the deviation from the equilibrium position, $\underset{\sim}{R}_{\ell,\alpha}$, is then the instantaneous position of the core at some temperature T. Then

$$\begin{aligned} V_p(r) &= \sum_{\underset{\sim}{G},\alpha} V_\alpha(\underset{\sim}{G})\ S_\alpha(\underset{\sim}{G})\ e^{+i\underset{\sim}{G}\cdot\underset{\sim}{r}} \\ &= \sum_{\underset{\sim}{G}} (V_1(\underset{\sim}{G}) e^{-i\underset{\sim}{G}\cdot\underset{\sim}{R}_{\ell,1}} + V_2(\underset{\sim}{G})\ e^{-i\underset{\sim}{G}\cdot\underset{\sim}{R}_{\ell,2}})\ e^{+i\underset{\sim}{G}\cdot\underset{\sim}{r}} . \end{aligned} \tag{5.6}$$

Equation (5.6) is similar to Eqs. (2.9), (2.10) except now $\underset{\sim}{R}_{\ell,\alpha}$ differs from the $\underset{\sim}{R}^{\circ}_{\ell,\alpha}$ by $\delta\underset{\sim}{R}_{\ell,\alpha}$. We may expand $\delta\underset{\sim}{R}_{\ell,\alpha}$ in the phonon coördinates,

$$\begin{aligned} \delta\underset{\sim}{R}_{\ell,\alpha} &= \sum_{\underset{\sim}{q},t} \left(\frac{\hbar}{2M_\alpha\ N\omega_{\underset{\sim}{q}t}}\right)^{1/2} (\underset{\sim}{\epsilon}_{\underset{\sim}{q},t,\alpha}\ a_{\underset{\sim}{q},t}\ e^{i\underset{\sim}{q}\cdot\underset{\sim}{R}^{\circ}_{\ell,\alpha}} \\ &\quad + \underset{\sim}{\epsilon}_{\underset{\sim}{q},t,\alpha}\ a_{\underset{\sim}{q},t}\ e^{-i\ \underset{\sim}{q}\cdot\underset{\sim}{R}^{\circ}_{\ell,\alpha}} . \end{aligned} \tag{5.7}$$

We recall from Chapter II that the pseudo-wavefunction $|\phi_v\rangle$ is expanded in plane waves and the eigenvalues are obtained by diagonalizing the truncated Hamiltonian matrix in this plane wave representation, it is clear then that the ensemble averaging process $\langle\ \rangle_{av}$, in Eq. (5.3), necessary for finite temperature calculations, brings in only an additional multiplicative factor of $\langle e^{-i\ G\cdot\delta R_{\ell,\alpha}}\rangle_{av}$ in the zero temperature structure factors in the Hamiltonian. Glauber[46] had shown that for a general m-real-phonon process,

$$1/m!\ \ A^m\ e^{\ (1/2\ \langle\chi_j|A^2|\ \chi_j\rangle_{av})} = 1/m!\ \ A^m\ e^{-W} \tag{5.8}$$

where

$$A = e^{i(\underset{\sim}{k}-\underset{\sim}{k}')\ \cdot\ \delta\underset{\sim}{R}_{\ell\ \alpha}}$$

and

$$W_\alpha\ (|\underset{\sim}{k}-\underset{\sim}{k}'|T) = 1/2 \sum_{\underset{\sim}{q},t} \frac{\hbar}{2M_\alpha N\ \omega_{\underset{\sim}{q},t}} (2\bar{n}_{\underset{\sim}{q},t}+1)$$

$$|(\underset{\sim}{k}-\underset{\sim}{k}') \cdot \underset{\sim}{\epsilon}_{\underset{\sim}{q},t,\alpha}|^2 , \tag{5.9}$$

and $\bar{n}_{\underset{\sim}{q},t}$ is the average occupation number of phonons in the mode $\underset{\sim}{q}$, t and ℓ^{-2W} the usual Debye-Waller factor. To take care of the self energy correction to the zero temperature band energies, we include all the processes where virtual phonons are emitted and reabsorbed, that is only zero-real-phonon processes are included in our finite temperature calculation, therefore the finite temperature pseudo-Hamiltonian matrix element in the plane wave representation is,

$$\mathcal{H}_{\underset{\sim}{k}'s',\underset{\sim}{k}s} = p^2/2m\ \delta_{\underset{\sim}{k}',\underset{\sim}{k}}\ \delta_{s',s} + \sum_{\alpha=1}^{2} e^{-i(\underset{\sim}{k}'-\underset{\sim}{k})\cdot\tau_\alpha}$$

$$e^{-W_\alpha}\ (|\underset{\sim}{k}'-\underset{\sim}{k}|,T) \times [V_\alpha\ (|\underset{\sim}{k}'-\underset{\sim}{k}|)\ \delta_{s's}$$

$$-i\ (\hat{k}'\times\hat{k})\ \lambda_\alpha \cdot \underset{\sim}{\sigma}_{s's}] . \tag{5.10}$$

As we have remarked earlier, this expression only differs from its zero temperature analog Eq. (2-22) by the presence of the square root of Debye-Waller factor, e^{-W}, in the structure factor. We may now define the finite temperature structure factor

$$S_\alpha(T) = e^{-i(\underset{\sim}{k}'-\underset{\sim}{k})\cdot\underset{\sim}{\tau}_\alpha}\quad e^{-W(|\underset{\sim}{k}'-\underset{\sim}{k}|,T)} , \tag{5.11}$$

we recall from Chapter II that $\underset{\sim}{\tau}_1 = (0,0,0)a$ and $\underset{\sim}{\tau}_2 = (0.5,0.5,0.5)a$ for the IV and VI atoms respectively.

B. Calculation

1. Evaluation of the Debye-Waller Factor

We first turn to the evaluation of W $(|\underset{\sim}{G}|,T)$ in Eq. (5.9), $(\underset{\sim}{k}'-\underset{\sim}{k})$

is now the reciprocal lattice vector, $\underset{\sim}{G}$. Substituting

$$2\bar{n}_{\underset{\sim}{q},t} + 1 = \frac{2}{e^{(\hbar\omega_{\underset{\sim}{q},t}/k_BT)} - 1} + 1$$

$$= \coth(\hbar\omega_{\underset{\sim}{q}\cdot t}/2k_BT) \qquad (5.12)$$

into Eq. (5.9), yields

$$W_\alpha(|\underset{\sim}{G}|,T) = 1/2 \sum_{q,t} \frac{\hbar}{2M_\alpha N} \frac{\coth(\hbar\omega_{\underset{\sim}{q},t}/2k_BT)}{\omega_{\underset{\sim}{q},t}} |\underset{\sim}{G}\cdot\underset{\sim}{\epsilon}_{\underset{\sim}{q},t,\alpha}|^2$$

$$= \frac{N\Omega}{2(2\pi)^3} \sum_t \int \frac{\hbar}{2M_\alpha N} \frac{\coth(\hbar\omega_{\underset{\sim}{q},t}/2k_BT)}{\omega_{\underset{\sim}{q},t}} |\underset{\sim}{G}\cdot\underset{\sim}{\epsilon}_{\underset{\sim}{q},t,\alpha}|^2\, d^3\underset{\sim}{q}\,. \qquad (5.13)$$

Now we may write

$$W_\alpha(|\underset{\sim}{G}|, T) = 1/2\, G^2 \langle\delta R^2_{\underset{\sim}{\ell}\,\alpha}\rangle_{av} \qquad (5.14)$$

since the ensemble average over phonon states of $\langle\delta R^2_{\underset{\sim}{\ell},\alpha}\rangle$ is, using the definition of $\delta R_{\underset{\sim}{\ell},\alpha}$ in Eq. (5.7),

$$\langle\delta R^2_{\underset{\sim}{\ell},\alpha}\rangle_{av} = \sum_{\substack{\underset{\sim}{q},\underset{\sim}{q}'\\ t,t'}} \frac{\hbar}{2NM_\alpha}(\omega_{\underset{\sim}{q}t}\,\omega_{\underset{\sim}{q}'t'})^{-1/2}$$

$$\Big(\langle n_{\underset{\sim}{q},t}|\, \underset{\sim}{\epsilon}_{\underset{\sim}{q},t,\alpha}\cdot\underset{\sim}{\epsilon}^{*}_{\underset{\sim}{q}',t',\alpha}\, a_{\underset{\sim}{q},t}\, a^{\dagger}_{\underset{\sim}{q}',t'}|n_{\underset{\sim}{q},t}\rangle_{av}$$

$$+ \langle n_{\underset{\sim}{q},t}|\underset{\sim}{\epsilon}^{*}_{\underset{\sim}{q},t,\alpha}\cdot\underset{\sim}{\epsilon}_{\underset{\sim}{q}',t'\alpha}\, a^{\dagger}_{\underset{\sim}{q},t}\, a_{\underset{\sim}{q}'t'}|n_{\underset{\sim}{q},t}\rangle_{av}\Big)$$

$$= \frac{N\Omega}{(2\pi)^3} \sum_t \int \frac{\hbar}{2M_\alpha N} \frac{\coth(\hbar\omega_{\underset{\sim}{q},t}/2k_BT)}{\omega_{\underset{\sim}{q},t}}$$

$$|\underset{\sim}{\epsilon}_{\underset{\sim}{q},t,\alpha}|^2 \quad d^3\underset{\sim}{q}\,. \qquad (5.15)$$

Keffer[47,48] has evaluated the $\underset{\sim}{q}$ integral over the Brillouin zone numerically using the PbTe phonon spectrum $\omega_{q,t}$ and polarization vectors $\underset{\sim}{\epsilon}_{\underset{\sim}{q},t,\alpha}$

obtained by Cochran et al.[49] In Table 5 we tabulate Keffer's result[47,48] at various temperatures for Pb and Te in PbTe. The tabulated results have a common zero point motion contribution to each $\langle \delta R^2_{\ell,\alpha} \rangle_{av}(T)$ substracted out because our method to determine the band energies at $T = 0°$ involves potentials obtained by fitting a few gaps to experiment and therefore presumably already contains the zero point motion.

2. Modification of Hamiltonian Matrix Elements

Since $W_{Pb}(|\underset{\sim}{G}|, T)$ is not equal to $W_{Te}(|\underset{\sim}{G}|, T)$, the property of the vanishing of symmetric form factors for odd $|\underset{\sim}{G}|^2$ and antisymmetric form factors for even $|\underset{\sim}{G}|^2$ (discussed in Chapter II, Eq.s (2.30)-(2.35)) is no longer valid. For finite temperatures, one needs $V^S(|\underset{\sim}{G}|^2 = 3, 11)$ and $V^A(|\underset{\sim}{G}|^2 = 4, 8, 12)$ as well as those required for the zero temperature calculation, namely $V^S(|\underset{\sim}{G}|^2 = 4, 8, 12)$ and $V^A(|\underset{\sim}{G}|^2 = 3, 11)$. These five additional form factors are obtained merely by an interpolation and extrapolation scheme using the form factors formerly used. To be specific, given the four values of $V^S(|G|^2 = 4, 8, 12)$ and $V^S(|G|^2 = 16) = 0$, we fit a smooth curve with a polynomial of order three to them and then interpolate $V^S(|G|^2 = 3, 11)$. The same procedure is applied to the set of V^A's.

Finally, to obtain the total temperature dependence of the band energies in our calculation, we must include the lattice expansion with increasing temperature. The change in lattice constant, a, modifies the Hamiltonian matrix element in the following terms: (1) the kinetic energy term scales as a^{-2} since $\underset{\sim}{k}$ is expressed in units of $(2\pi/a)$, (2) all the reciprocal lattice vectors scale as $(2\pi/a)$ by definition and (3) the pseudopotential form factors

$$V_\alpha(\underset{\sim}{G}) = 2/\Omega \int V_\alpha(|\underset{\sim}{r}|)\, e^{-i\underset{\sim}{G}\cdot\underset{\sim}{r}}\, d^3\underset{\sim}{r} \qquad (5.16)$$

scale according to $\underset{\sim}{G}$ in the exponential as well as the volume factor $\Omega = a^3/4$. We have assumed $V_\alpha(|\underset{\sim}{r}|)$, the atomic pseudopotential to be independent of temperature in our scaling process, which is the rigid ion assumption.

We now have all the tools to calculate the temperature dependent band structure within the framework of the pseudopotential method; the actual procedure used for PbTe will be summarized:

(a) We determined the lattice constant a(T) for various temperatures in the range T = 0° to 400°K from experimental data.[50] The experimental expansion coefficient $\alpha = 1/a\left(\Delta a/\Delta_T\right)\big|_P$ is constant above T = 100°K and has the value $1.97\times10^{-6}/°K$; for temperatures less than 100°K, α increases with temperature. The lattice constants a(T) are listed in Table 6.

(b) For the Debye-Waller effect, we now need both symmetric and anti-symmetric structure factors (S^S and S^A, respectively) and the symmetric and antisymmetric form factors (V^S and V^A) at values of $|G|^2 = (2\pi/a)^2$ (3, 4, 8, 11, 12). Therefore the $|G|^2$ are explicitly functions of lattice constant a (in the discussion for the zero temperature band structure calculation in Chapter II, we have assumed implicitly that $\underset{\sim}{G}$ is measured in units of $(2\pi/a)$ and for abbreviation, used $|G|^2 = 3,4,8,11,12$).

(c) The form factors are scaled and interpolated to the $|G|^2$ appropriate to the lattice constant a(T), as described in earlier part of this section.

(d) The Debye-Waller factors ,

$$e^{-W_\alpha(|G|,\,T)} = e^{-1/2\, G^2 \langle \delta R^2_{\ell,\alpha} \rangle_{av}} \qquad (5.17)$$

are included in the structure factors so that for PbTe,

$$
\begin{aligned}
S_{Pb}\,(G,T) &= e^{-i\underset{\sim}{G}\cdot\underset{\sim}{\tau}_{Pb}}\; e^{-W_{Pb}(|\underset{\sim}{G}|^2,T)} \\
S_{Te}\,(G,\,T) &= e^{-\underset{\sim}{G}\cdot\underset{\sim}{\tau}_{Te}}\; e^{-W_{Te}(|\underset{\sim}{G}|^2,\,T)}
\end{aligned}
\tag{5.18}
$$

and

$$
\begin{aligned}
S^S(G,T) &= (S_{Pb}\,(G,\,T) + S_{Te}\,(G,T))/2 \\
S^A(G,T) &= (S_{Pb}\,(G,\,T) - S_{Te}\,(G,T))/2i
\end{aligned}
\tag{5. 19}
$$

(e) The truncated pseudo-Hamiltonian matrix with modifications (a), (b), (c) and (d) is then diagonalized as discussed in Chapter II to obtain the energies for finite temperature. The reference zero temperature form factors are tabulated in Table .

C. Temperature Dependent Energy Gap Results

Table 7 gives the temperature dependence of the fundamental energy gap at L, $E_g(T)$ is given at nine temperatures in the temperature range T = 100°K to 400°K. The curve $E_g(T)$ versus T is also plotted in Fig. 11 together with optical experimental data.[31] Although we obtain the correct positive sign for the temperature coefficient $\partial E_q/\partial T|_P$, its magnitude in the temperature range where $E_q(T)$ is almost linear is only 2.25×10^{-4} eV/°K between T = 100°K and T = 300°K. Optical experiments[31] give 4.1×10^{-4} eV/°K between T = 100°K and 350°K. We believe that our formulation of the theory of the temperature dependence of the energy band structure is correct, but the agreement between experiment and theory is not entirely satisfactory. Therefore, in the following section, we consider various possible causes for the low theoretical value of $\partial E_q/\partial T|_P$.

D. Discussion of $\partial E_g/\partial T|_P$

(1) Our first attempt at a more detailed analyses is to separate the lattice effect from the Debye-Waller effect in the temperature dependent band structure calculation. Since the two convenient variables for theoretical calculations of the temperature coefficient are volume and temperature, the temperature coefficient for the energy gap $E_g(V,T)$ at constant pressure is:

$$\left.\frac{\partial E_g(V,T)}{\partial T}\right|_P = \left.\frac{\partial E_g(V,T)}{\partial V}\right|_T \left.\frac{\partial V}{\partial T}\right|_P + \left.\frac{\partial E_g(V,T)}{\partial T}\right|_V . \tag{5.20}$$

We first consider the first term in Eq. (5.18). Suppose we scale the five zero temperature form factors $V^S(G^2 = 4,8,12)$ and $V^A(|G|^2 = 3,11)$ to values corresponding to lattice constants at $(T = 100°K)$ and $a(T = 300°K)$, we obtain

$$[E_g(T = 300°K) - E_g(T = 100°K)]/200°K = 1.75\times10^{-4}\ eV(°K)^{-1}. \tag{5.21}$$

If we use the experimentally measured pressure dependence of the energy gap,[42] compressibility and expansion coefficient to obtain the first term in (Eq. 5.20), we deduce a value of 1.7×10^{-4} $eV(°K)^{-1}$ for PbTe. The agreement between theory and experiment results is very good for lattice effect alone.

Now we turn to the second term $\partial E_g/\partial T|_V$ in Eq. (5.20). We take the set of zero temperature form factors $V^S(|G|^2 = 4,8,12)$ and $V^A(|G|^2 = 3,11)$ and interpolate $V^S(|G|^2 = 3,11)$ and $V^A(|G|^2 = 4,8,12)$. Then we put in the Debye-Waller factors in the structure factors S^S and S^A. The lattice constant a is constrained to be the zero temperature value throughout this calculation. The gap energies as a function of temperature coming from this Debye-Waller effect alone are given in Table 8. We note the following points from Table 8:

(a) The temperature coefficient is very small, on the average, it is about a factor of three to four smaller than that coming from the lattice effect alone. It is therefore necessary to keep values of E_g, expressed in eV up to the fourth decimal point in Table 8 in order to get a picture of how the energy gap moves with respect to temperature. We recall that our calculation gives convergence of energies with respect to E_1 (Chapter II) only up to 0.1 eV, but when we are looking at one point of the Brillouin zone, the size of the Hamiltonian matrix to be diagonalized remains constant from one temperature calculation to another and our comparison of energies up to the fourth decimal place is valid in this context.

(b). It is interesting to note that the temperature coefficient (arising only from the Debye-Waller effect) $\partial E_g/\partial T|_V$ is positive from 0° to 300°K, but for temperatures greater than 300°K, $\partial E_g/\partial T|_V$ becomes negative. Our calculation stopped at 400°K, limited by the unavailability of Debye-Waller factors for higher temperatures. If we were to predict that $\partial E_g/\partial T|_V$ will continue to be negative for higher temperatures, then this will bring about a flattening of the theoretical curve $E_g(T)$ (the total temperature dependent energy gap, containing both lattice and Debye-Waller effects) versus T (refer to Fig. 11). This flattening of $E_g(T)$ versus T above 350°K is a characteristic feature of the experimental data.

From the above discussion it is apparent that the discrepancy between the total theoretical temperature coefficient and the experimental result arises mainly from the Debye-Waller and not the lattice effect. We proceed to investigate the sensitivity of the Debye-Waller temperature effect as a function of different sets of form factors used.

(2) In this section, temperature coefficient will always mean $\partial E_g/\partial T|_V$, that is, that part arising only from the Debye-Waller effect.

In Table 9, we list the six energy levels at L and their temperature coefficients from our empirical pseudopotential band structure calculation, together with energies given by other pseudopotential, $(\underset{\sim}{k},\underset{\sim}{p})$APW and OPW calculations by various authors.[11,51-53] A close examination of this table shows the following: 1) The energies of all levels, except one level (lower L_6^+) from our calculation agrees well with those given by other calculations, our lower L_6^+ level is on the average 1.3 eV lower than all other calculations; 2) the temperature coefficients of all levels is positive, but the L_6^- level at the conduction edge has a slightly larger $\partial E/\partial T|_V$ than the L_6^+ level at the valence edge, giving rise to a net $\partial E_g/\partial T|_V$ of 0.3 eV/°K between T = 100°K and 300°K (the experimental value is 2.4×10^{-4} eV/°K); 3) the lower L_6^+ level has an extraordinary large temperature coefficient $\partial E/\partial T|_V = 12.8\times10^{-4}$ eV/°K, as compared with values between 4.5 to 7.9×10^{-4} eV/°K for the other energy levels. From these three points, our first guess is to relate the energy separation of our lower L_6^+ level from the gap to the smallness of our gap temperature coefficient. We are therefore led to the following question: if we were to bring the lower L_6^+ level up to be near the gap, as in other theoretical calculations, can the large temperature coefficient of the lower L_6^+ have the effect of enlarging the gap temperature coefficient? To obtain an answer to the above, we did the following analysis.

Given the original set of form factors, which we hereafter call set A, we vary the form factors one at a time to move the lower L_6^+ level, keeping the ordering of all the energy levels at L unchanged. It turns out that only the two antisymmetric form factors $V^A(3)$ and $V^A(11)$ have any appreciable effect on the lower L_6^+ level,

$$\left| \frac{\partial E_{L_6^+}}{\partial V^A} \right| \approx 2 \text{ to } 3, \text{ and} \tag{5.22}$$

variations of $V^S(4)$ and $V^S(8)$ have almost no effect on this lower L_6^+ level,

$$\left| \frac{\partial E_{L_6^+}}{\partial V^S(12)} \right| \lesssim 2. \tag{5.23}$$

The upper limit of variation of each form factor is ±0.01 Rydberg and the lower limit is governed by the criterion that the ordering of the energy levels at L should be the same, regardless of the set of form factors used and the temperatures. In particular, we require the valence band edge to have symmetry L_6^+ and the conduction band edge to have symmetry L_6^-. The resultant set of form factors used, labeled set A through set G, are tabulated in Table 10. For each set of form factors, we calculated the energies at L for $T = 0°$, 100° and 300°K, including only the Debye-Waller effect for the finite temperature calculations. We obtain the temperature coefficient $\partial E/\partial T|_V$ between 100°K and 300°K for each level from the finite temperature calculations. These results are listed in Table 11.

We then analyze the data tabulated in Table 11 by correlating the temperature coefficients of the top valence and the bottom conduction bands with the energy separations: top valence L_6^+ to lower L_6^+, top valence L_6^+ to upper L_6^-, bottom conduction L_6^- to lower L_6^+ and bottom conduction L_6^- to upper L_6^-. The temperature coefficient of the gap, $\partial E_g/\partial T|_V$ is

$$\left.\frac{\partial E_g}{\partial T}\right|_V = \left.\frac{\partial E_{L_6^-}}{\partial T}\right|_V - \left.\frac{\partial E_{L_6^+}}{\partial T}\right|_V . \qquad (5.24)$$

We observe the following as a result of our analysis:

(a) The temperature coefficient of each energy level fluctuate only slightly as different sets of form factors are used, it varies at most by 1.4×10^{-4} eV/°K.

(b) Sets B and C correspond to a variation of the form factors $V^A(3)$ from set A, and results for sets A, B and C indicate that when both the upper L_6^- and lower L_6^+ levels are close to the top valence and bottom conduction levels, $\partial E_g/\partial T|_V$ increases. Sets D and E correspond to the variation of the form factor $V^A(11)$ from set A; results for sets A, D and E show that $\partial E_g/\partial T|_V$ is larger when upper L_6^- level is close to top valence L_6^+ and lower L_6^+ level is close to bottom conduction L_6^-. These results also require that the two L_6^- conduction levels be kept apart as well as the two L_6^+ valence band be kept apart for a larger $\partial E_g/\partial T|_V$. Lastly, sets F and G correspond to the variation of $V^S(12)$ from set A. The energies and temperature coefficients for the sets A, F, G indicate that in order to obtain a larger $\partial E_g/\partial T|_V$, the upper L_6^- level should be close to the top valence L_6^+. However, the energy difference between the upper L_6^- and top valence L_6^+ should be large, and the splitting between the lower L_6^+ and the bottom conduction L_6^- should also be large.

From (b) it is obvious that no simple conclusion may be drawn from the analysis: results from sets A, B, E and sets A, F, G are contradictory However, if we now correlate the temperature coefficient with the gap size, we get a consistent trend. In Table 12 we tabulate the energy gap in one column and the temperature coefficient in another; these numbers invariably show that a smaller gap corresponds to a larger temperature coefficient within each group of form factor sets: {A,B,C} {A,D,E} and {A,F,G}. Each group of form factor sets correspond to variation of one form factor by not more than 0.01 Ry. from the starting set A. Table 12 essentially shows that if we were to keep a gap size consistent with experiment, then we have to accept a gap temperature coefficient which is far smaller than the experimentally predicted value, on the other hand, if we were to allow the gap to go to nearly zero (0.02 eV) then $\partial E_g/\partial T|_V$ reaches a value of 1.3×10^{-4} eV/°K, closer to the experimentally predicted value 2.4×10^{-4} eV/°K than our original 0.3×10^{-4} eV/°K. It appears that we cannot do too much better since we need to keep the correct ordering of the top valence and bottom conduction bands at L. We will have futher discussion on this point later, in the meantime, we turn once again to the temperature effect coming from lattice expansion.

(3) We have shown in section (1) of this chapter that our theoretical calculation of the contribution to $\partial E_g/\partial T|_P$ from lattice expansion alone using form factor set (A) gives good agreement with experiment. Our calculation gives $(\partial E_g/\partial V|_T)$ $(\partial V/\partial T|_P)$ = 1.75×10^{-4} eV/°K while experiment yields 1.7×10^{-4} eV/°K. In section (2) we show that by variation of certain form factors, we may improve our $\partial E_g/\partial T|_V$ calculation

(which is the other contribution to $\partial E_g/\partial T|_P$, the total temperature coefficient of the gap); it is therefore necessary that we also investigate the sensitivity of the lattice contribution to $\partial E_g/\partial T|_P$ by the variation of the form factors. To take care of only the lattice effect, we take the lattice constants at 100°K and 300°K, scale the zero temperature form factor sets A through G to these two temperatures and calculate the energies at L for these temperatures. In Table 13, we tabulate the resultant temperature coefficients $\partial E/\partial V|_T \ \partial V/\partial T|_P$ for the levels at L between 100°K and 300°K using the sets of form factors A through G (i.f. Table 11 for $\partial E/\partial T|_V$). Table 13 indicates the following:

(a) Unlike the Debye-Waller effect, the lattice effect gives comparable values of the temperature coefficients for all levels at L. They all fall between (3 to 5)$\times 10^{-4}$ eV/°K; there is not one level that has an exceptionally large value of $\partial E/\partial V|_T \ \partial V/\partial T|_P$ as in the case of $\partial E/\partial T|_V$.

(b) The fluctuation of the temperature coefficients arising from lattice effects as we vary the sets of form factors is only half of that found for Debye-Waller effect, that is, these temperature coefficients are not very sensitive to the variation of form factors. The range of values of $\partial E_g/\partial V|_T \ \partial V/\partial T|_P$ is between (1.35 to 2.2)$\times 10^{-4}$ eV/°K as the form factors are varied up to 0.01 Ry., all are in fair agreement with the experimental value 1.7$\times 10^{-4}$ eV/°K.

Based on the above investigations, we conclude this chapter with the following remarks: (1) the correct ordering of bands at the gap which we obtained from the empirical pseudopotential method is crucial in giving the correct positive sign for the temperature coefficient for

PbTe. For SnTe, because Debye-Waller factors are not available at present, we have only calculated the lattice effect term. The value of $\partial E_g(V,T)/\partial V|_T \; \partial V/\partial T|_P$ for SnTe using the expansion coefficient

$$\alpha = 1/(3V)\, \partial V/\partial T|_P = 1.75\times 10^{-6}\ (^\circ K)^{-1}, \qquad (5.25)$$

is -1.48×10^{-4} eV/°K for the temperature coefficient due only to the lattice effect. The sign is again correct for SnTe, (2) the magnitude of $\partial E_g/\partial T|_V$ is very sensitive to the starting set of zero temperature form factors. Because of the non-uniqueness of the pseudopotential in fitting the band gaps, it is conceivable that if we had used more form factors as parameters (e.g. the antisymmetric form factor for high $|G|^2$), we could have attained the objective of both keeping the correct ordering and magnitude of gap and getting the right magnitude for the temperature coefficient $\partial E_g/\partial T|_P$. The exceptionally large energy difference (as compared with other calculations[11,51-53]) between the lower and valence L_6^+ levels for form factors sets A through G (Tables 9 and 11) may well be the cause of the discrepancy between calculated value of $\partial E_g/\partial T|_V$ and experimental value; that is, a set of form factors which give the proper energies of all levels at L could give the desired magnitude for the temperature coefficient $\partial E_g/\partial T|_P$. (3) Table 9 indicates that $\partial E_g/\partial T|_V$ (a small number) was obtained by substracting the energy coefficients of one level from the other (both of which are large numbers) so that any discrepancy in the calculated temperature coefficient of each level is magnified by a factor of 2 in the resultant gap temperature coefficient. A correction of 10-20% in the temperature coefficient of the valence L_6^+ and conduction L_6^- levels arising from form factors change Table 11 could give the correct $\partial E_g/\partial T|_V$.

VI. DEFORMATION POTENTIAL

A. Introduction

In early investigations into the possibility of superconductivity in degenerate superconductors, Cohen's[54,55] calculations indicated that superconductivity was possible in highly doped, many-valley semiconductors with large static dielectric constants. It was expected that these materials would be superconducting around 0.1°K, that the superconducting transition temperature T_c, should be a function of carrier density, n, and that these materials would be type II superconductors.

Both SnTe and GeTe have the desired normal state properties and experiments have shown these materials[2,4] to be superconducting. In addition, experiments[56-58] on powdered samples and heat capacity measurement have firmly established that superconductivity was a bulk effect in these materials. The first superconducting property to be explored in detail was the dependence of the superconducting transition temperature on carrier concentration, $T_c(n)$; for both GeTe and SnTe superconductivity was found to exist over a wide range of carrier concentration.[3,4,58]

A recent calculation[32,59] of $T_c(n)$ has been made. This calculation involves one adjustable parameter ξ, the deformation potential which measures the strength of the electron-phonon coupling for electrons which are scattered from one Fermi-surface pocket near L to another by exchanging a short wavelength phonon. The inversion symmetry of the rock-salt structure forbids non-zero electron-phonon matrix elements connecting electrons from one L point to another in the Brillouin zone. We have therefore investigated the matrix elements between electronic states in the L valleys near the L point.

B. Theory and Calculation

We take our band structure pseudopotential and a rigid ion model for the electron-phonon interaction,

$$\mathcal{H}'_{\text{e-ph}} = \sum_{\ell,\alpha} \underset{\sim}{\nabla} V_{\ell\alpha}(\underset{\sim}{r} - \underset{\sim}{R}^{\circ}_{\ell\alpha}) \cdot \delta \underset{\sim}{R}_{\ell\alpha} \tag{6.1}$$

where $V_{\ell\alpha}(\underset{\sim}{r} - \underset{\sim}{R}^{\circ}_{\ell\alpha})$ is the pseudopotential about the atom core in its equilibrium position with lattice index ℓ, and basis index α, $\delta \underset{\sim}{R}_{\ell\alpha}$ is the displacement of the core from its equilibrium position $R^{\circ}_{\ell\alpha}$. We Fourier analyze $V_{\ell\alpha}$ and express the displacement $\delta \underset{\sim}{R}_{\ell\alpha}$ in terms of phonon co-ordinates:

$$V_{\ell\alpha}(\underset{\sim}{r} - \underset{\sim}{R}_{\ell\alpha}) = \frac{\Omega}{(2\pi)^3} \int V_{\underset{\sim}{q}\,\alpha}\, e^{i\underset{\sim}{q}\cdot(\underset{\sim}{r} - \underset{\sim}{R}_{\ell\alpha})}\, d^3\underset{\sim}{q} \tag{6.2}$$

$$\delta \underset{\sim}{R}_{\ell\alpha} = (\hbar/2M_{\alpha} N \omega_{\underset{\sim}{Q},t})^{1/2}\, \underset{\sim}{\epsilon}_{t\alpha}\, e^{i\underset{\sim}{Q}\cdot\underset{\sim}{R}^{\circ}_{\ell\alpha}} = A_{t\alpha}\, \underset{\sim}{\epsilon}_{t\alpha}\, e^{i\underset{\sim}{Q}\cdot\underset{\sim}{R}^{\circ}_{\ell\alpha}} \tag{6.3}$$

where M_{α} is the mass of the α^{th} atom in the primitive cell with volume Ω, $\underset{\sim}{Q}$ is the wave vector of the t^{th} mode phonon with frequency $\omega_{\underset{\sim}{Q},t}$ and $\underset{\sim}{\epsilon}_{t\alpha}$ is the polarization vector connected with the t^{th} mode and the α^{th} atom. Putting Eq. (6.2) and (6.3) into Eq. (6.1) we get,

$$\mathcal{H}'_{e-\alpha} = \sum_{\ell\ \alpha} \frac{\Omega}{(2\pi)^3} \int d^3\underset{\sim}{q}\, (i\underset{\sim}{q}\cdot\underset{\sim}{\epsilon}_{t\alpha})\, A_{t\alpha} V_{q\alpha}\, e^{i\underset{\sim}{q}\cdot(\underset{\sim}{r}-\underset{\sim}{R}^{\circ}_{\ell\alpha})}\, e^{i\underset{\sim}{Q}\cdot\underset{\sim}{R}^{\circ}_{\ell\alpha}} \tag{6.4}$$

If we write $\underset{\sim}{R}^{\circ}_{\ell\alpha} = \underset{\sim}{R}^{\circ}_{\ell} + \underset{\sim}{\tau}_{\alpha}$, then Eq. (6.4) becomes

$$\sum_{\alpha} \frac{\Omega}{(2\pi)^3} \int d^3\underset{\sim}{q}\, (i\underset{\sim}{q}\cdot\underset{\sim}{\epsilon}_{t\alpha})\, A_{t\alpha} V_{\underset{\sim}{q}\alpha}\, e^{i\underset{\sim}{q}\cdot\underset{\sim}{r}}\, e^{i(\underset{\sim}{Q}-\underset{\sim}{q})\cdot\underset{\sim}{\tau}_{\alpha}} \sum_{\ell} e^{i(\underset{\sim}{Q}-\underset{\sim}{q})\cdot R^{\circ}_{\ell}}$$

$$= \sum_{\alpha} \frac{\Omega}{(2\pi)^3} \int d^3\underset{\sim}{q}\, (i\underset{\sim}{q}\cdot\underset{\sim}{\epsilon}_{t\alpha})\, A_{t\alpha} V_{\underset{\sim}{q}\alpha}\, e^{i\underset{\sim}{q}\cdot\underset{\sim}{r}}\, e^{i(\underset{\sim}{Q}-\underset{\sim}{q})\cdot\tau_{\alpha}}\, N\, \delta_{\underset{\sim}{G},\underset{\sim}{Q}-\underset{\sim}{q}}, \tag{6.5}$$

where we used $\sum_{\ell} e^{i(\underset{\sim}{Q}-\underset{\sim}{q})\cdot \underset{\sim}{R}_{\ell}^{\circ}} = N\, \delta_{\underset{\sim}{G},\underset{\sim}{Q}-\underset{\sim}{q}}$. (6.6)

In Eq. (6.5) $\underset{\sim}{G}$ is the reciprocal lattice vector and N the number of primitive cells in the crystal. Since the sum over lattice sites gives us the Kronecker delta relation $\underset{\sim}{q} = \underset{\sim}{Q} - \underset{\sim}{G}$, the integral over $\underset{\sim}{q}$ values may be written as a sum over discrete reciprocal lattice vectors $\underset{\sim}{G}$, converting the sum to an integral. Equation (6.5) becomes

$$\mathcal{H}'_{\ell-} = \sum_{\alpha,\underset{\sim}{G}} i \left(\frac{\hbar}{2M_{\alpha} N\omega_{q,t}}\right)^{1/2} \underset{\sim}{\epsilon}_{t\alpha} \cdot (\underset{\sim}{Q}-\underset{\sim}{G})\, V_{\underset{\sim}{Q}-\underset{\sim}{G},\alpha}\, e^{i(\underset{\sim}{Q}-\underset{\sim}{G})\cdot \underset{\sim}{r}} \times e^{i\underset{\sim}{G}\cdot \underset{\sim}{\tau}_{\alpha}} . \tag{6.7}$$

If an electron is scattered from a state $\phi_{\underset{\sim}{k}s}$ in one valley to a state $\phi_{\underset{\sim}{k}'\underset{\sim}{s}'}$ in another valley by a phonon with wave vector $\underset{\sim}{Q}$, the deformation potential ξ for crystal with only one type of atom is defined[54] as

$$\left| \langle \phi_{\underset{\sim}{k}'s'} \right| \mathcal{H}'_{e-ph} \left| \phi_{\underset{\sim}{k}s} \rangle \right|^2 = \frac{\nu\hbar\xi^2}{2MN\omega_{\underset{\sim}{Q}}} \tag{6.8}$$

where ν is the degeneracy of the phonon which connects the $\underset{\sim}{k}S$ and $\underset{\sim}{k}'s'$ states. In our calculation, we have used the pseudo-wavefunctions for $\phi_{\underset{\sim}{k}s}$ and as we mentioned before, the pseudopotential in the perturbation $\mathcal{H}'_{e-ph}$ term. Because the initial and final electronic states of an intervalley process both lie on the Fermi surface, with the same energy, Sham's theorem[60] justifies our use of the pseudo-wavefunctions and pseudopotential in the calculation of the electron-phonon matrix element, the results will be the same if we were to use the real potential and the real electronic wave functions.

To modify the definition (6.8) to our case of two atoms per primitive cell, we may write $\bar{M} = (M_1+M_2)/2$ in place of M on the right side of Eq. (6.8), then the deformation potential ξ may be written out explicity,

$$\xi^2 = 1/\nu \, \Big| \sum_{\alpha,\underset{\sim}{G}} (\bar{M}/M_\alpha)\; i\; \underset{\sim}{\epsilon}_{t\alpha} \cdot (\underset{\sim}{Q}-\underset{\sim}{G})\; V_{\underset{\sim}{Q}-\underset{\sim}{G},\alpha}\; e^{i\underset{\sim}{G}\cdot\underset{\sim}{\tau}_\alpha}$$

$$\times \; \langle \phi_{\underset{\sim}{k}'s'} | \; e^{i(\underset{\sim}{Q}-\underset{\sim}{G})\cdot r} \; | \phi_{\underset{\sim}{k}s} \rangle \Big|^2 . \tag{6.9}$$

From Chapter II, Eq. (2.33) and Eq. (6.9), one obtains

$$\xi^2 = \Big| \sum_{\underset{\sim}{G}} [\bar{M}/M_1)\; i\underset{\sim}{\epsilon}_{t1} \cdot (\underset{\sim}{Q}-\underset{\sim}{G})\; V_{\underset{\sim}{Q}-\underset{\sim}{G},1}$$

$$\pm \; (\bar{M}/M_2)\; i\; \underset{\sim}{\epsilon}_{t2} \cdot (\underset{\sim}{Q}-\underset{\sim}{G})\; V_{\underset{\sim}{Q}-\underset{\sim}{G},2} \;]$$

$$\times \; \langle \phi_{\underset{\sim}{k}'s'} | \; e^{i(\underset{\sim}{Q}-\underset{\sim}{G})\cdot\underset{\sim}{r}} \; | \phi_{\underset{\sim}{k}s} \rangle \Big|^2 , \tag{6.10}$$

where the plus sign apply to the even $\underset{\sim}{G}$'s and the minus to the odd $\underset{\sim}{G}$'s in the summation.

We outline the actual computation of Eq. (6.10)

(1) Since the pseudo-wavefunctions $\phi_{\underset{\sim}{k}s}$ are expanded in about thirty plane waves in our band structure calculation,

$$\phi_{\underset{\sim}{k}s} = \sum_{\underset{\sim}{G}'} C^{\underset{\sim}{k}s}_{\underset{\sim}{G}'} \; e^{i(\underset{\sim}{k}+\underset{\sim}{G}')\cdot\underset{\sim}{r}} \; ; \tag{6.11}$$

the matrix element in Eq. (6.11) becomes

$$\langle \phi_{\underset{\sim}{k}'s'} | e^{i(\underset{\sim}{Q}-\underset{\sim}{G})\cdot\underset{\sim}{r}} \; | \phi_{\underset{\sim}{k}s} \; \rangle$$

$$= \sum_{\underset{\sim}{G}',\underset{\sim}{G}''} C^{\underset{\sim}{k}'s'*}_{\underset{\sim}{G}'} \; C^{\underset{\sim}{k}s}_{\underset{\sim}{G}''} \; e^{i[-(\underset{\sim}{k}'+\underset{\sim}{G}')+(\underset{\sim}{Q}-\underset{\sim}{G})+(\underset{\sim}{k}+\underset{\sim}{G}'')] \cdot \underset{\sim}{r}}$$

$$= \sum_{\underset{\sim}{G}'} C^{\underset{\sim}{k}'s'*}_{\underset{\sim}{G}'} \; C^{\underset{\sim}{k}s}_{\underset{\sim}{G}''} \; \delta_{\underset{\sim}{G}'', \, -[(\underset{\sim}{Q}-\underset{\sim}{G})+(\underset{\sim}{k}-\underset{\sim}{k}') \, - \, \underset{\sim}{G}']} \, . \tag{6.12}$$

(2) The wave vector of the intervalley phonon $\underset{\sim}{Q} = \underset{\sim}{k}'-\underset{\sim}{k}$ is not a reciprocal lattice vector, we therefore need to interpolate given values of $V^S(\underset{\sim}{G})$ and $V^A(\underset{\sim}{G})$ to obtain $V^S(\underset{\sim}{Q}-\underset{\sim}{G})$ and $V^A(\underset{\sim}{Q}-\underset{\sim}{G})$ since in pseudopotential

band structure calculation, pseudopotential form factors are only given for reciprocal lattice vectors $\underset{\sim}{G}$ such that $|G|^2 < 12$.

(3) Whereas V^S and V^A are convenient in the band structure calculation, clearly, V_1 and V_2 are useful in this calculation, therefore, we need the decomposition

$$\begin{aligned} V_1(\underset{\sim}{Q}-\underset{\sim}{G}) &= V^S(\underset{\sim}{Q}-\underset{\sim}{G}) + V^A(\underset{\sim}{Q}-\underset{\sim}{G}) \\ V_2(\underset{\sim}{Q}-\underset{\sim}{G}) &= V^S(\underset{\sim}{Q}-\underset{\sim}{G}) - V^A(\underset{\sim}{Q}-\underset{\sim}{G}) \end{aligned} \tag{6.13}$$

(4) We consider the scattering of electrons from one valley to another by coupling to a longitudinal acoustic phonon, that is, we consider cases where the polarization vectors $\underset{\sim}{\epsilon}_{t\alpha}$ are parallel to the phonon wave vector $\underset{\sim}{Q}$.

(5) The wave vector $\underset{\sim}{Q}$ connecting the L point $(1/2,1/2,1/2)\ 2\pi/a$ and $L' = (-1/2,1/2,1/2)\ 2\pi/a$ is:

$$\underset{\sim}{Q} = L' - L = (1,0,0)\ 2\pi/a \tag{6.14}$$

Therefore an X phonon connects two non-equivalent L points, the coupling by this particular $\underset{\sim}{Q}$ is identically zero simply because the electronic wave functions have definite parity at the symmetry point L while all phonons in rocksalt structure are odd. This prediction is verified by our computation, we obtain $\xi=0$ for the $\underset{\sim}{Q} = (1,0,0)\ 2\pi/a$ coupling.

For both PbTe and SnTe, the Fermi surface of holes centers about the L points in the Brillouin zone. If we define $|\Delta\underset{\sim}{k}|$ to be the mean radius of the Fermi surface from the L point in $\underset{\sim}{k}$ space, then $|\Delta\underset{\sim}{k}| \leq 0.045\ (2\pi/a_{PbTe})$ for typical PbTe carrier concentrations up to $8\times10^{18}\ cm^{-3}$. For SnTe, $|\Delta\underset{\sim}{k}|$ is about $0.11\ (2\pi/a_{SnTe})$ for moderate concentrations $10^{20}\ cm^{-3}$ (higher carrier concentrations in the range

10^{21} cm^{-3} are also common for SnTe). The estimated values of $|\Delta \underset{\sim}{k}|$ are derived from our Fermi surface calculations, which we discussed in Chapter IV. For our calculation of ξ^2 the initial and final electronic state $\phi_{\underset{\sim}{k}s}$, $\phi_{\underset{\sim}{k}'s'}$ are allowed to have $\underset{\sim}{k}$ vectors such that

$$\begin{aligned} &|\underset{\sim}{k} - (1/2,1/2,1/2)\, 2\pi/a\,| \lesssim |\Delta \underset{\sim}{k}| \\ \text{and} \quad &|\underset{\sim}{k}' - (-1/2,1/2,1/2)\, 2\pi/a\,| \lesssim |\Delta \underset{\sim}{k}| \,. \end{aligned} \tag{6.15}$$

(6) Since $|\Delta \underset{\sim}{k}| \ll |\underset{\sim}{G}|$, a reciprocal lattice vector, the phonon exchanged when electrons are scattered from a state near L to a final state near L' will have a wave vector $\underset{\sim}{Q}$ very close to that of an X phonon that is, the phonons that are coupled to the electrons within the Fermi surface are essentially zone edge phonons which give modes involving essentially the motion of only one atom (when there are two in the primitive cell). We label mode a such that

$$\begin{aligned} \underset{\sim}{\epsilon}_{a1} &= 1 \\ \underset{\sim}{\epsilon}_{a2} &= 0 \end{aligned} \quad , \tag{6.16}$$

and mode b such that

$$\begin{aligned} \underset{\sim}{\epsilon}_{b1} &= 1 \\ \underset{\sim}{\epsilon}_{b2} &= 0 \end{aligned} \quad . \tag{6.17}$$

We assume these two modes for all our computations.

C. Results and Discussions

For SnTe we select six states at random near L, these are indexed by the $\underset{\sim}{k}$ vectors, $\underset{\sim}{k}_1$ through $\underset{\sim}{k}_6$ which are listed in Table 14. The corresponding states in another valley centered about L' will be labeled by $\underset{\sim}{k}_1'$ through $\underset{\sim}{k}_6'$ respectively. The primed $\underset{\sim}{k}_1'$ are related to the unprimed ones as the following:

$$\begin{aligned} &\text{if} && \underset{\sim}{k}_i = (k_x, k_y, k_z) \\ &\text{then} && \underset{\sim}{k}_i' = (-k_x, k_y, k_z). \end{aligned} \qquad (6\text{-}18)$$

We allow electrons to scatter from the unprimed to the primed valley. The resultant deformation ξ obtained for the two phonon modes a and b for several scattering processes in SnTe are tabulated in Table 15. The corresponding $\underset{\sim}{k}$ vectors and deformation potentials results for PbTe are tabulated in Tables 16 and 17 respectively.

Both SnTe and PbTe give ξ on the order of a few electron volts. Although our calculation verifies the selection rule forbidding scattering from L to L', as we obtain zero for this process, it seems that as soon as $|\Delta\underset{\sim}{k}|$ is slightly larger than zero, ξ already jumps to a finite value. Our calculation shows no consistent trend, e.g. ξ does not appear to increase from zero as $|\Delta\underset{\sim}{k}|^2$ when the initial and final states are $|\Delta\underset{\sim}{k}|$ from L and L' in the range of $|\Delta\underset{\sim}{k}|$ which we considered here. In addition, we found that the value of ξ is enhanced if we were to allow the pseudopotential to tail off more slowly, i.e. to allow higher $|\underset{\sim}{G}|^2$ cut off values for the pseudopotential form factors. These led us to believe that our calculation of ξ in this pseudopotential formulation only gives qualitatively reliable results. There probably is little profit in a complete quantitative calculation of the value of ξ, obtained by averaging all the electron scatterings over the Fermi surface It is sufficient for our purpose that the value of ξ we obtained for SnTe is roughly the same as that used by Allen and Cohen[32,59] (their values of ξ were 2.35, 2.63 eV) to explain the superconductivity properties of

SnTe. This calculation and the results in Tables 15 and 17 indicates that ξ is roughly the same in both materials, regardless of the ordering of the bands at the band edge. The fact that PbTe is not superconducting is probably due to the smaller carrier concentration in PbTe and not due to the fact that the electron phonon coupling in PbTe is weaker than that in SnTe.

APPENDIX A

Simplification and Evaluation of the Spin-Orbit Matrix Element

We evaluate the terms $\underset{\sim}{\Lambda}^{p-p}$, $\underset{\sim}{\Lambda}^{c-p}$, $\underset{\sim}{\Lambda}^{p-c}$ and $\underset{\sim}{\Lambda}^{c-c}$ from Eq. (2.19) in turn.

$$\begin{aligned}\underset{\sim}{\Lambda}^{p-p} &= \frac{\hbar}{4m^2c^2}\ \frac{1}{N\Omega}\int e^{-i\underset{\sim}{k}'\cdot\underset{\sim}{r}}\ \nabla\underset{\sim}{V}\times p\ e^{i\underset{\sim}{k}\cdot\underset{\sim}{r}}\,d^3\underset{\sim}{r}\\ &= (\hbar/4m^2c^2\ N\Omega)\ I_{pp}, \qquad (A.1)\end{aligned}$$

Where N is the number of primitive cells and Ω is the volume of each cell, $1/N\Omega$ comes from the normalization of the plane wave states, and

$$\begin{aligned}I_{pp} &= \int e^{-i\underset{\sim}{k}'\cdot\underset{\sim}{r}}\ \nabla\underset{\sim}{V}\times\underset{\sim}{p}\ e^{i\underset{\sim}{k}\cdot\underset{\sim}{r}}\,d^3\underset{\sim}{r}\\ &= \int\nabla\underset{\sim}{V}\times\hbar\underset{\sim}{k}\ e^{i(\underset{\sim}{k}-\underset{\sim}{k}')\cdot\underset{\sim}{r}}\,d^3\underset{\sim}{r}\\ &= -\hbar\int\underset{\sim}{k}\times[\ \underset{\sim}{\nabla}\ (V\ e^{i(\underset{\sim}{k}-\underset{\sim}{k}')\cdot\underset{\sim}{r}}) \qquad (A.2)\\ &\quad - V\,\underset{\sim}{\nabla}\ (e^{i(\underset{\sim}{k}-\underset{\sim}{k}')\cdot\underset{\sim}{r}})\ d^3\underset{\sim}{r}\ ]\ .\end{aligned}$$

The first term of the integral in (A.2) is zero because if we expand the real crystal potential in reciprocal lattice vectors,

$$V(r) = \sum_{\underset{\sim}{G}} U(G)\ e^{i\underset{\sim}{G}\cdot\underset{\sim}{r}}, \qquad (A.3)$$

This term becomes

$$\begin{aligned}&-\hbar\underset{\sim}{k}\times\int\sum_{\underset{\sim}{G}} i(\underset{\sim}{k}-\underset{\sim}{k}'+\underset{\sim}{G})\ U(G)\ e^{i(\underset{\sim}{k}-\underset{\sim}{k}'+\underset{\sim}{G})\cdot\underset{\sim}{r}}\,d^3\underset{\sim}{r}\\ &= -\hbar\underset{\sim}{k}\times\sum_{\underset{\sim}{G}} i(\underset{\sim}{k}-\underset{\sim}{k}'+\underset{\sim}{G})\ U(G)\ \delta\ (\underset{\sim}{k}-\underset{\sim}{k}'+\underset{\sim}{G})\ N\Omega = 0, \qquad (A.4)\end{aligned}$$

where we have used the notation U(G), for the Fourier transform of the crystal potential to distinguish it from V(G), that of the pseudopotential in Chapter II.

The second term in (A.2) is

$$i\hbar\mathbf{k} \times (\mathbf{k}-\mathbf{k}') \int V(\mathbf{r})\; e^{i(\mathbf{k}-\mathbf{k}')\cdot\mathbf{r}}\, d^3\mathbf{r} = i\hbar\,(\mathbf{k}'\times\mathbf{k}) \sum_{\alpha} U_{\alpha}(|\mathbf{k}-\mathbf{k}'|) \times S_{\alpha}(\mathbf{k}'-\mathbf{k})\, N\Omega \tag{A.5}$$

where $S_{\alpha}(\mathbf{k}'-\mathbf{k})$ is the structure factor as defined in Eqs. (2.9) and (2.10) and $U_{\alpha}(\mathbf{k}-\mathbf{k}')$ is the fourier transform of the atomic crystal potential centered about the α^{th} atom in a primitive cell. Therefore,

$$\mathbf{\Lambda}^{p-p} = \frac{i\hbar^2}{4m^2c^2}\,(\mathbf{k}'\times\mathbf{k}) \sum_{\alpha} S_{\alpha}(\mathbf{k}-\mathbf{k}')\, U_{\alpha}(|\mathbf{k}-\mathbf{k}'|). \tag{A.6}$$

For the calculation of $\mathbf{\Lambda}^{p-c}$, $\mathbf{\Lambda}^{c-p}$ and $\mathbf{\Lambda}^{c-c}$ we make the following assumptions: (1) Whenever $\mathbf{\Lambda}$ operates on a core state, $|b_t\rangle$, $\mathbf{\Lambda}$ is approximated by

$$\sum_{i,\alpha} \xi\,(|\mathbf{r}-\mathbf{R}_{i\alpha}|)\, \boldsymbol{\ell} \tag{A.7}$$

where i is the primitive cell index and α the basis index, $\boldsymbol{\ell}$ is the dimensionless angular momentum operator and

$$\xi\,(|\mathbf{r}-\mathbf{R}_{i\alpha}|) = \frac{\hbar^2}{4m^2c^2}\,\frac{1}{|\mathbf{r}-\mathbf{R}_{i\alpha}|}\,\frac{\partial V(|\mathbf{r}-\mathbf{R}_{i\alpha}|)}{\partial|\mathbf{r}-\mathbf{R}_{i\alpha}|} \tag{A.8}$$

$V(|\mathbf{r}-\mathbf{R}_{i\alpha}|)$ is just the atomic crystal potential centered about the α^{th} atom in the i^{th} primitive cell.

(2) The core states are expressed in terms of spherical harmonics Y_{ℓ}^{m} and a radical function $R_{n\ell}$, that is

$$b_t = b_{n\ell m}(\mathbf{r}) = \sum_{i,\alpha} R_{n\ell}\,(|\mathbf{r}-\mathbf{R}_{i\alpha}|)\, Y_{\ell}^{m}(\theta,\phi) \tag{A.9}$$

Both assumptions (1) and (2) are based on the fact that spin-orbit interaction is localized near the core so that the core states are little changed from atomic orbitals. (3) The plane wave states may also be expressed in spherical harmonics Y_ℓ^m so that:

$$e^{i\underset{\sim}{k}\cdot\underset{\sim}{r}} = \sum_{\ell=0}^{\infty} i^\ell \, [4\pi(2\ell+1)]^{1/2} \; j_\ell\,(kr)\; Y_{\ell k}, \qquad (A.10)$$

where $Y_{\ell k}(\theta,\phi)$ is the spherical harmonic with the rotation index $m = \ell_z = 0$ with z defined in the $\underset{\sim}{k}$ direction.

Now we have to evaluate three types of integrals: $\langle \underset{\sim}{k}'|b_t\rangle$, $\langle \underset{\sim}{k}'|\underset{\sim}{\Lambda}|b_t\rangle$ and $\langle b_t|\Lambda|b_t\rangle$; the matrix elements $\underset{\sim}{\Lambda}^{c-p}$, $\underset{\sim}{\Lambda}^{p-c}$ and $\underset{\sim}{\Lambda}^{c-c}$ are just different combinations of these integrals. We first note that one always gets a structure factor from these integrals, merely due to the fact that the core states $|b_t\rangle$ is a sum over all lattice and basic sites (Eq. A.9). For example,

$$\langle k'|b_t\rangle = \frac{1}{(N\Omega)^{1/2}} \int e^{-ik'\cdot r} \sum_{i,\alpha} R_{n\ell}\,(|\underset{\sim}{r}-\underset{\sim}{R}_{i\alpha}|)\;\; Y_\ell^m\,(\theta,\phi)d^3\underset{\sim}{r} \qquad (A.11)$$

with a change of variable from $\underset{\sim}{r}-\underset{\sim}{R}_{i\alpha}$ to $\underset{\sim}{r}'$, Eq. (A.11) becomes

$$\frac{1}{(N\Omega)^{1/2}} \sum_{i,\alpha} e^{-i\underset{\sim}{k}'\cdot\underset{\sim}{R}_{i\alpha}} \; e^{-i\underset{\sim}{k}'\cdot\underset{\sim}{r}'} \; R_{n\ell}\,(r')\; Y_\ell^m\,(\theta,\phi)\; d^3\underset{\sim}{r}' \qquad (A.12)$$

It is the $e^{-i\underset{\sim}{k}'\cdot\underset{\sim}{R}_{i\alpha}}$ in Eq. (A.12) which gives rise to a structure factor. The reminaing intergration is over the atomic co-ordinate $\underset{\sim}{r}'$.

All three integrals can also be factored into a radial and an angular part, we examine the radial part first. $\langle b_t|\underset{\sim}{k}'\rangle$ involves a radial integral as follows:

$$\int i^\ell \,[4\pi(2\ell+1)]^{1/2} \;\; j_\ell\,(k'r')\; R_{n\ell}\;\;(r')r'^2\, dr' = B_{n\ell}\,(k') \qquad (A.13)$$

Similarly, $\langle b_t|\underset{\sim}{\Lambda}|\underset{\sim}{k}\rangle$ involves, putting aside the structure factor the radial integral

$$A_n\,(k) \;=\; \int i^\ell [4\pi(2\ell+1)]^{1/2}\, j_\ell\,(kr')\;\xi\,(r')\;R_{n\ell}\,(r')\;r'^2\,dr' \qquad (A.14)$$

From Eq.s (2.19), (A.13) and (A.14) we see that $\underset{\sim}{\Lambda}^{p-c}$ and $\underset{\sim}{\Lambda}^{c-p}$ involves a summation over all the core states (indexed by quantum numbers n and ℓ) of products $A_{n\ell}(\underset{\sim}{k})\; B_{n\ell}{}^*(\underset{\sim}{k}')$ and $A^*_{n\ell}(k')\; B_{n\ell}(k)$ respectively. By making the reasonable assumption that

$$\langle b_{t'} | \underset{\sim}{\Lambda} | b_t \rangle = \Delta^{t}_{s-o} \; \delta_{t,t'} , \tag{A.15}$$

i.e the atomic spin-orbit splitting of the energy level t=nℓ, we may write $\underset{\sim}{\Lambda}^{c-c}$ also in terms of summation of products $B^{*}_{n\ell}(k')\, B_{n\ell}(k)\Delta^{n\ell}_{s-o}$.

Our first attempt in solving these integrals involved the use of Slater orbitals[61] for the core state, these orbitals are essentially nodeless hydrogen- like wavefunctions with an effective charge. We used the Coulomb potential with the same effective charge in the spin orbit interaction $\xi\,(\underset{\sim}{r})\ \underset{\sim}{\Lambda}\cdot\underset{\sim}{\sigma}$. We found from the evaluation of these integrals that $\underset{\sim}{\Lambda}^{c-c}$ is at least three orders of magnitude larger than the $\underset{\sim}{\Lambda}^{p-c}$ terms which in turn are orders of magnitude larger than $\underset{\sim}{\Lambda}^{p-p}$. This result is not surprising since the spin-orbit interaction is a localized one and we would therefore expect the core-core contribution, $\underset{\sim}{\Lambda}^{c-c}$, to dominate.

Now we consider the angular matrix element

$$\langle Y_{\ell' \underset{\sim}{k}'} \,|\, \underset{\sim}{\ell} \,|\, Y_{\ell \underset{\sim}{k}} \rangle = \langle Y_{\ell \underset{\sim}{k}'} | \underset{\sim}{\ell} | Y_{\ell \underset{\sim}{k}} \rangle \tag{A.16}$$

in the $\underset{\sim}{\Lambda}^{c-c}$ term. We define a set of right hand orthonormal cartesian axes $\{c_1, c_2, c_3\}$ such that

$$\underset{\sim}{k}' = k'\,\hat{c}_3 \tag{A.17}$$

$$\underset{\sim}{k} = k \sin\theta\,\hat{c}_1 + k\cos\theta\,\hat{c}_3 , \tag{A.18}$$

and the operator $\underset{\sim}{\ell}$ is;

$$\begin{aligned} \ell &= \ell_x \hat{c}_1 + \ell_y\,\hat{c}_2 + \ell_z\,\hat{c}_3 \\ &= \frac{(\ell_+ + \ell_-)}{2}\,\hat{c}_1 + \frac{(\ell_+ - \ell_-)}{2i}\,\hat{c}_2 + \ell_z\,\hat{c}_3 . \end{aligned} \tag{A.19}$$

In other words, $\underset{\sim}{k}$ may be obtained from $\underset{\sim}{k}'$ by a rotation operation $R(\alpha,\beta,\gamma)$ of $\alpha = \gamma = 0$, $\beta = \theta$, where α, β,γ are the usual Eulerian angles as defined by Rose[62] and Tinkham.[63] The wavefunction $Y_{\ell m}$ with $\underset{\sim}{k}$ taken to be its z axis transforms to the primed system, where $\underset{\sim}{k}'$ is along the c_1 axis as follows:

$$R(\alpha.\beta.\gamma) \quad Y_{\ell m} \;=\; \sum_{m'} Y'_{\ell m'} \, D^{(\ell)}\,(\alpha,\beta,\gamma)_{m'm} \qquad (A.20)$$

For $\ell=1$

$$D^{(1)}\,(0,\theta,0) \;=\; \begin{pmatrix} \frac{1+\cos\theta}{2} & -\frac{\sin\theta}{\sqrt{2}} & \frac{1-\cos\theta}{2} \\ \frac{\sin\theta}{\sqrt{2}} & \cos\theta & -\frac{\sin\theta}{\sqrt{2}} \\ \frac{1-\cos\theta}{2} & \frac{\sin\theta}{\sqrt{2}} & \frac{1+\cos}{2} \end{pmatrix} \qquad (A.21)$$

then

$$\begin{aligned} \underset{\sim}{\ell} Y_{1\underset{\sim}{k}} \;=\; & \left[\frac{(\ell_+ + \ell_-)}{2}\,\hat{c}_1 + \frac{(\ell_+ - \ell_-)}{2i}\,\hat{c}_2 + \ell_z\,\hat{c}_3 \right] \\ & \left(-\frac{\sin\theta}{\sqrt{2}}\, Y'_{11} + \cos\theta\, Y'_{10} + \frac{\sin}{\sqrt{2}}\, Y'_{1-1} \right) \\ =\; & \hat{c}_1/2\,\left(\sqrt{2}\cos\theta\, Y'_{11} + \sqrt{2}\cos\theta\, Y'_{1-1} \right) \\ & + \frac{\hat{c}_2}{2i}\left(2\sin\theta\, Y'_{10} + \sqrt{2}\cos\theta\, Y'_{11} - \sqrt{2}\cos\theta\, Y'_{1-1} \right) \\ & + \hat{c}_3\left(-\frac{\sin\theta}{\sqrt{2}}\, Y'_{11} + \frac{\sin\theta}{\sqrt{2}}\, Y'_{1-1} \right). \end{aligned} \qquad (A.22)$$

The matrix element of Eq. (A.16) becomes

$$\langle Y_{\ell \underset{\sim}{k}'} | \underset{\sim}{\ell} | \, Y_{\ell \underset{\sim}{k}} \rangle \;=\; i\,\hat{c}_2 \sin\theta \;=\; -i\,(\hat{k}'\times\hat{k}), \qquad (A.23)$$

which is the contribution to the Λ^{c-c} term from angular integration.

ACKNOWLEDGMENTS

I am deeply grateful to Professor M. L. Cohen, my research advisor, for his guidance and encouragement throughout the course of this work. I would also like to express my deep appreciation to Professor C. Kittel, who, with insight and patience, directed the early part of my research.

It is a pleasure to thank all the graduate students and post-doctoral physicsits in the Solid-State Theory Group, who helped me to understand and resolve innumerable questions in the course of this work. In particular, discussions with Professor C. Y. Fong, Dr. Phil Allen, Bob Cahn, John Walter and Professor S. Bowen are most appreciated.

I thank Professor A. Bienenstock for helpful discussions and for very kindly supplying me with the Debye-Waller factors for PbTe which he and Dr. C. Keffer calculated. Thanks are also due to Professor T. K. Bergstresser and Dr. S Bloom for supplying me with the details of their spin-orbit calculation.

The financial support of the National Science Foundation and the United States Atomic Energy Commission is gratefully acknowledged.

REFERENCES

1. M. L. Cohen and T. K. Bergstresser, Phys. Rev. 141, 789 (1966).
2. See discussion section of M.L. Cohen, Rev. Mod. Phys. 36 240 (1964).
3. R. A. Hein, J. W. Gibson, R. Mazelsky, R. C. Miller, and J. K. Hulm, Phys. Rev. Letters 12, 320 (1964).
4. R. A. Hein, J. W. Gibson, R. S.Allgaier, B. B. Houston, Jr., R. L. Mazelsky, and R. C. Miller, Proc IX Int. Conf. Low Temp. Physic, (1965), p. 604.
5. M. Cardona and B. L. Greenaway, Phys. Rev. 133, A1685 (1964).
6. L. L. Chang, P. J. Stiles, and L. Esaki, IBM J. Res. Develop. 10, 484 (1966). L. Esaki and P. J. Stiles, Phys. Rev. Letters 16, 1108 (1966).
7. J. F. Butler and A. R. Calawa, in "Physics of Quantum Electronics," edited by P. L. Kelley, B. Lax and P. E. Tannenwald (McGraw-Hill Book Co., Inc., New York), (1966), p. 458.
8. K. F. Cuff, M. R. Ellett, and C. D. Kuglin, Proceedings of the International Conference on the Physics of Semiconductors, Exeter (1962), p. 316.

8a. J. R. Burke, Jr., B. Houston, and H. T. Savage, Proceedings of the International Conference on the Physics of Semiconductors, Kyoto, (1966), p. 384.

J. R. Burke, Jr., R. S. Allgaier, B. B. Houston, J. Babiskin, and P. G. Siebenmann, Phys. Rev. Letters 14, 360 (1965).

9. J. O. Dimmock, I. Melngailis, and A. J. Strauss, Phys. Rev. Letters 16, 1193 (1966).
10. I. Weinberg and J. Callaway, Nuovo Cimento 24, 190 (1962).
11. J. B. Conklin, Jr., L. E. Hounson, and G. W. Pratt, Jr., Phys. Rev. 137, A1282 (1965).

12. J. R. Burke, Jr., R. S. Allgaier, B. B. Houston, Jr., J. Babiskin, and P. G. Siebenmann, Bull. Am. Phys. Soc. 10, 350 (1965).

13. P. J. Lin, W. Saslow, and M. L. Cohen, Solid State Commun. 5, 893 (1967).

14. M. L. Cohen, P. J. Lin, D. M. Rossler, and W. C. Walker, Phys. Rev. 155, 992 (1967).

15. M. Y. Au Yang and M. L. Cohen, Phys. Rev. 178, 1358 (1969).

16. M. Y. Au Yang and M. L. Cohen, Phys. Rev. 178, 1279 (1969).

17. M. L. Cohen and V. Heine, to be published in Solid States Physics, edited by F. Seitz, D. Turnbull, and H. Ehrenreich (Academic Press Inc., New York).

18. G. Weisz, Phys. Rev. 149, 504 (1966).

19. F. Heiman and S. Skillman, Atomic Structure Calculations (Prentice-Hall, Inc., Englewood Cliffs, N.J.), (1963).

20. P. Lowdin, J. Chem. Phys. 19, 1396 (1951).

21. D. Brust, Phys. Rev. 134, A1337 (1964).

22. F. Herman, C. D. Kuglin, K. F. Cuff, and R. L. Kontum, Phys. Rev. Letters 11, 541 (1963).

23. A. O. E. Animalu and V. Heine, Phil. Mag. 12, 1249 (1965).

24. J. R. Dixon and H. R. Riedl, Phys. Rev. 138, A873 (1965).

25. R. S. Allgaier, J. Appl. Phys. 32, 2185 (1961).

26. R. S. Allgaier and B. B. Houston, Jr., J. Appl. Phys. 37, 302 (1966). B. B. Houston and R. S. Allgaier, Bull. Am. Phys. Soc. 9, 293 (1964).

27. H. R. Riedl, Phys. Rev. 127, 162 (1962).

28. R. J. Brebrick and A. J. Strauss, Phys. Rev. 131, 104 (1963).

29. J. A. Kafalas, R. F. Brebrick, and A. J. Strauss, Appl. Phys. Letters 4, 93 (1964).

30. B. A. Efimova, V. I, Kaidanov, B. Ya. Moizhes, and I. A. Chernick, Fiz. Tveid. Tela, 7, 2524 (1965) (English transl. Soviet Phys.-Solid State 7, 2032 (1966).

31. R. N. Tauber, A. A. Machonis, and I. B. Cadoff, J. Appl. Phys. 31, 4855 (1966).

32. M. L. Cohen, Y. Tung, and P. B. Allen, J. de Physique 29, C4-163 (1968).

33. Y. W. Tung and M. L. Cohen, Phys. Rev. 180, 823 (1969). Y. W. Tung and M. L. Cohen, Phys. Letters A 29, 236 (1969).

34. L. Van Hove, Phys. Rev. 89, 1189 (1953).

35. J. C. Phillips, Phys. Rev. 104, 1263 (1956).

36. J. C. Phillips, Solid State Physics edited by F. Seitz and D. Turnbull, (Academic Press, New York and London), 18, 55 (1966).

37. D. E. Aspnes and M. Cardona, Bull. Am. Phys. Soc. 13, 27 (1968).

38. See discussion section of J. R. Burke, Jr., B. Houston, H. T. Savage, J. Babiskin and P. G. Siebenmann, J. Phys. Soc. Japan 21, Supplement 384 (1966).

39. W. Saslow, T. K. Bergstresser, C. Y. Fong, M. L. Cohen, and D. Brust Solid State Comm. 5, 167 (1967).

40. C. Y. Fong, W. Saslow, and M. L. Cohen, Phys. Rev. 168, 992 (1968).

41. J. R. Burke, Private communication.

42. V. Prakash, Ph. D. Thesis, Harvard University, (1967).

43. S. C. Yu, Ph.D. Thesis, Harvard University, (1964).

44. S. C. Yu and H. Brooks, unpublished manuscript.

45. J. M. Ziman, Electrons and Phonons (Oxford University Press, London), (1960).

46. R. J. Galuber, Phys. Rev. 84, 395 (1951) and ibid 98, 1692 (1955).

47. C. Keffer, PhD. Thesis, Harvard University, (1969).

48. C. Keffer, T. M. Hayers and A. Bieneustock, to be published.

49. W. Cochran, R. A. Cowley, G. Dolling, and M. M. Elcombe, Proc. Roy. Soc. (London) A293, 433 (1966).

50. B. Houston, R. E. Stranka, and H. S. Belson, J. of Appl. Phys. 39, 3913 (1968).

51. D. D. Buss, and N. J. Parada, to be published.

52. P. J. Lin and L. Kleinman, Phys. Rev. 142, 478 (1965).

53. F. Herman, R. L. Kortum, I. B. Ortenburger, and J. P. Van Dyke, Journal de Physique 29, C4-62 (1969).

54. M. L. Cohen, Phys. Rev. 134, A511 (1964).

55. M. L. Cohen, Rev. Mod. Phys. 36, 240 (1964).

56. L. Finegold, Phys. Rev. Letters, 13, 233 (1964).

57. L. Finegold, J. K. Hulm, R. Mazelsky, N. E. Phillips, and B. B. Triplett, Ann. Finn. Acad. Sci., Ser., A6, 129 (1966).

58. J. K. Hulm, C. K. Jones, D. W. Deis, H. A. Fainbank, and P. A. Lawless, Phys. Rev. 169, 388 (1968).

59. P. B. Allen and M. L. Cohen, Phys. Rev. 177, 704 (1969).

60. L. J. Sham, Proc. Phys. Soc. 78, 895 (1961).

61. J. C. Slater, Phys. Rev. 36, 57 (1930).

62. M. E. Rose, "Elementary Theory of Angular Momentum," (J. Wiley and Sons Book Co., Inc. New York), (1957).

63. M. Tinkham, "Group Theory and Quantum Mechanics," (McGraw Hill Book Co., Inc. New York), (1964).

TABLE CAPTIONS

1. Pseudopotential form factors for SnTe, PbTe and GeTe.
2. Energies and symmetries of critical points and interband transitions associated with prominent optical structure at low energy for SnTe, GeTe and PbTe.
3. Lattice constants, form factors and spin-orbit parameters for SnTe, PbTe and (Sn,Pb)Te alloys.
4. Fermi energy (ϵ_f) in SnTe and PbTe as a function of hole carrier concentrations (p).
5. Calculated vibrational amplitudes $\langle \delta R^2_{\ell\alpha} \rangle_{Av}$,(with zero point motion contribution subtracted out), for Pb and Te in PbTe. (These values were obtained from Refs. 47 and 48).
6. Lattice constants a(T) for PbTe determined from experiment (see ref. 50)
7. Total temperature dependence of the energy gap at L.
8. Temperature dependence of the energy gap at L caused only by the Debye-Waller effect.
9. Energy and temperature coefficients ($\partial E/\partial T|_V$) of L levels for PbTe given by the EPM and energies of L levels given by other methods (Refs. 51, 52, 53, 11).
10. Sets of form factors used in the investigation of the temperature coefficients $\partial E/\partial T|_V$.
11. Zero temperature energy levels and temperature coefficients $\partial E/\partial T|_V$ between T = 100°K and 300°K at L using form factor sets A through G.
12. Energy band gap E_g and its temperature coefficient $\partial E_g/\partial T|_V$ for form factor sets A through G.

13. Temperature coefficients ($\partial E/\partial V|_T \; \partial V/\partial T|_P$) between T = 100°K and 300°K for energy levels at L using form factor sets A through G.
14. The $\underset{\sim}{k}$ vectors of the initial electronic states used in the calculation of the deformation potential for SnTe.
15. Deformation potential ξ for SnTe.
16. The $\underset{\sim}{k}$ vectors of the initial electronic states used in the calculation of the deformation potential for PbTe.
17. Deformation potential ξ for PbTe.

TABLE 1

Material	$V^S(4)$	$V^S(8)$	$V^S(12)$	$V^A(3)$	$V^A(11)$
SnTe	-.232 Ry	-.024	.018	.055	.023
PbTe	-.241	-.0352	.017	.052	.021
GeTe	-.245	-.022	.032	.060	.017

TABLE 2

Material	Band Energy (in eV)	Critical Point Symmetry	Band Transition
SnTe	0.33	M_0	$L(5 \rightarrow 6)$
	0.85	M_0	$\Sigma(5 \rightarrow 6)$
	1.75	M_0	$\Sigma(5 \rightarrow 7)$
	1.99	M_2	$\Delta(5 \rightarrow 6)$
	3.0	M_1	$\Sigma(4 \rightarrow 7)$
	3.02	M_2	$\Delta(4 \rightarrow 6)$
GeTe	0.23	M_0	$L(5 \rightarrow 6)$
	1.06	M_1	$\Sigma(5 \rightarrow 6)$
	1.81	M_1	$\Sigma(5 \rightarrow 7)$
	2.25	M_2	$\Delta(5 \rightarrow 6)$
	3.24	M_1	$\Sigma(4 \rightarrow 7)$
	3.57	M_2	$\Delta(4 \rightarrow 6)$
PbTe	0.18	M_0	$L(5 \rightarrow 6)$
	1.07	M_0	$\Sigma(5 \rightarrow 6)$
	1.27	M_0	$L(5 \rightarrow 7)$
	2.00	M_0	$\Sigma(5 \rightarrow 7)$
	2.02	M_2	$\Delta(5 \rightarrow 6)$
	2.78	M_2	$\Delta(4 \rightarrow 6)$
	3.1	M_1	$\Sigma(4 \rightarrow 7)$

TABLE 3

Material	Lattice Constant (in Å)	Form factors (in Rydbergs)					s-o Parameters	
		$V^S(4)$	$V^S(8)$	$V^S(12)$	$V^A(3)$	$V^A(11)$	λ^S	λ^A
PbTe	6.454	-.241	-.0352	.017	.052	.021	.033	-.0009
$Sn_{0.25}Pb_{0.75}Te$	6.4188	-.2388	-.0324	.01725	.05275	.0215	.00273	-.0008
$Sn_{0.5}Pb_{0.5}Te$	6.3835	-.2365	-.0296	.0175	.0535	.022	.00245	-.0006
$Sn_{0.75}Pb_{0.25}Te$	6.3483	-.2343	-.0268	.01775	.05425	.0225	.00218	-.0005
SnTe	6.313	-.232	-.024	.018	.055	.023	.0019	-.0003

TABLE 4

	PbTe		SnTe
$-\epsilon_F$(eV)	(10^{19} cm^{-3})	$-\epsilon_F$(eV)	(10^{20} cm^{-3})
0.02	0.08	.01	.02
0.04	0.56	.02	.06
0.05	0.61	.08	.70
0.06	0.77	.10	.90
0.09	1.69	.11	1.03
0.11	2.42	.12	1.16
0.14	3.82	.15	1.65

TABLE 5

Temperature °K	$\langle \delta R^2_{Pb} \rangle_{av}$ (units of 10^{-16} cm^2)	$\langle \delta R^2_{Te} \rangle_{av}$ (units of 10^{-16} cm^2)
0°	0	0
20°	.0006	.0002
40°	.002	.0008
100°	.007	.0036
140°	.0105	.0056
200°	.0157	.0086
240°	.0192	.0107
300°	.0244	.0138
340°	.0279	.0159
400°	.0332	.0189

TABLE 6

Temperature (°K)	a(T) in Å
0°	6.313
20°	6.4543
40°	6.4556
100°	6.4624
140°	6.4675
200°	6.4751
240°	6.4802
300°	6.4879
340°	6.4929
400°	6.5006

TABLE 7

Temperature (°K)	Energy gap at L(eV)
0°	0.181
20°	0.184
40°	0.19
100°	0.207
140°	0.218
200°	0.233
300°	0.252
340°	0.259
400°	0.269

TABLE 8

Temperature (°K)	Energy gap at L (eV)
0°	0.1807
20°	0.1833
40°	0.1877
100°	0.1941
140°	0.1974
200°	0.2004
300°	0.2007
340°	0.1997
400°	0.1993

TABLE 9

Energy level symmetry	Energy (eV) of $\underset{\sim}{k}\cdot\underset{\sim}{p}$ method[51]	Energy (eV) by pseudopotential method[52]	Energy (eV) by OPW method[53]	Energy (eV) by APW method[11]	Energy (eV) by EPM (this work)	Temperature coefficients (eV/°K) between T=100°K and 300°K from EPM
L_{45}^-	1.496	1.442	1.95	1.659	1.747	6.15×10^{-4}
L_6^-(upper L_6^-)	1.224	1.319	1.45	1.06	1.365	7.9×10^{-4}
L_6^-	0.34	0.217	0.25	0.122	0.181	5.95×10^{-4}
	GAP					
L_6^+	0	0	0	0	0	5.65×10^{-4}
L_{45}^+	-0.884	-0.748	-0.95	-0.9112	-0.909	4.5×10^{-4}
L_6^+(lower L_6^+)	-1.428	-1.197	-1.53	-1.536	-2.802	12.8×10^{-4}

TABLE 10

Set label	Form factors in Rydbergs				
	$V_s(4)$	$V_s(8)$	$V_s(12)$	$V_A(3)$	$V_A(11)$
A	-.241	-.0352	.017	.052	.021
B	-.241	-.0352	.017	.062	.021
C	-.241	-.0352	.017	.047	.021
D	-.241	-.0352	.017	.052	.011
E	-.241	-.0352	.017	.052	.024
F	-.241	-.0352	.027	.052	.021
G	-.241	-.0352	.007	.052	.021

TABLE 11

Set label	Symmetry label	0°K energy (eV) with energy reference shifted to valence band edge for each set	$\partial E/\partial T\|_V$ (10^{-4} eV/°K) between T=100°K and 300°K
A	L_{45}^-	1.75	6.15
	L_6^-	1.36	7.9
	L_6^-	0.18	5.95
	GAP		
	L_6^+	0	5.65
	L_{45}^+	-0.91	4.5
	L_6^+	-2.80	12.8
B	L_{45}^-	2.11	5.8
	L_6^-	1.75	7.45
	L_6^-	0.46	5.2
	GAP		
	L_6^+	0	6.55
	L_{45}^+	-1.18	5.0
	L_6^+	-3.07	13.3
C	L_{45}^-	1.55	6.45
	L_6^-	1.16	8.15
	L_6^-	0.02	6.4
	GAP		

Table 11 continued

Set label	Symmetry label	0°K energy (eV) with energy reference shifted to valence band edge for each set	$\partial E/\partial T\|_V$ (10^{-4} eV/°K) between T=100°K and 300°K
	L_6^+	0	5.2
	L_{45}^+	-0.79	4.25
	L_6^+	-2.68	12.6
D	L_{45}^-	2.155	5.65
	L_6^-	1.777	7.35
	L_6^-	0.7031	5.55
	GAP		
	L_6^+	0	6.4
	L_{45}^+	-0.695	4.55
	L_6^+	-2.578	12.9
E	L_{45}^-	1.625	6.35
	L_6^-	1.243	8.05
	L_6^-	0.028	6.1
	GAP		
	L_6^+	0	5.4
	L_{45}^+	-0.973	4.55
	L_6^+	-2.869	12.85
F	L_{45}^-	1.57	6.8
	L_6^-	1.20	8.35
	L_{6-}	0.128	6.5
	GAP		

Table 11 continued

Set label	Symmetry label	0°K energy (eV) with energy reference shifted to valence band edge for each set	$\partial E/\partial T\|_V$ (10^{-4} eV/°K) between T=100°K and 300°K
	L_6^+	0	5.55
	L_{45}^+	-1.052	4.95
	L_6^+	-2.898	12.9
G	L_{45}^-	1.919	5.55
	L_6^-	1.525	7.45
	L_6^-	0.227	5.5
	GAP		
	L_6^+	0	5.75
	L_{45}^+	-0.772	4.1
	L_6^+	-2.612	12.8

TABLE 12

Formfactor set	Variation of formfactor	Energy gap E_g (eV)	gap temperature coefficient $\partial E_g/\partial T|_V$ (10^{-4} eV/°K)
A		0.18	0.3
B	$V_A(3)$	0.46	-1.35
C		0.02	1.2
A		0.18	0.3
D	$V_A(11)$	0.703	-0.85
E		0.028	0.7
A		0.18	0.3
F	$V_s(12)$	0.128	0.95
G		0.227	-0.25

TABLE 13

Set label	Symmetry label	$\partial E/\partial V\|_T \ \partial V/\partial T\|_P$ 10^{-4} eV/°K	$\partial E_g/\partial V\|_T \ \partial V/\partial T\|_P$ (10^{-4} eV/°K)
A	L_{45}^-	-4.0	
	L_6^-	-4.2	
	L_6^-	-4.1	
	GAP		+1.75
	L_6^+	-5.85	
	L_{45}^+	-3.65	
	L_6^+	-5.15	
B	L_{45}^-	-3.9	
	L_6^-	-4.2	
	L_6^-	-4.0	
	GAP		+2.2
	L_6^+	-6.2	
	L_{45}^+	-3.65	
	L_6^+	-5.1	
C	L_{45}^-	-4.0	
	L_6^-	-4.2	
	L_6^-	-4.15	
	GAP		+1.6
	L_6^+	-5.75	
	L_{45}^+	-3.7	
	L_6^+	-5.15	

Table 13 continued

Set label	Symmetry label	$\partial E/\partial V\|_T \ \partial V/\partial T\|_P$ 10^{-4} eV/°K	$\partial E_g/\partial V\|_T \ \partial V/\partial T\|_P$ (10^{-4} eV/°K)
D	L_{45}^-	-3.9	
	L_6^-	-4.2	
	L_6^-	-4.25	
	GAP		+1.35
	L_6^+	-5.6	
	L_{45}^+	-3.7	
	L_6^+	-5.25	
E	L_{45}^-	-4.0	
	L_6^-	-4.25	
	L_6^-	-4.05	
	GAP		+1.9
	L_6^+	-5.95	
	L_{45}^+	-3.65	
	L_6^+	-5.15	
F	L_{45}^-	-3.7	
	L_6^-	-3.7	
	L_6^-	-4.2	
	GAP		+1.8
	L_6^+	-6.1	
	L_{45}^+	-3.35	
	L_6^+	-5.05	

Table 13 continued

Set label	Symmetry label	$\partial E/\partial V\|_T \ \partial V/\partial T\|_P$ 10^{-4} eV/°K	$\partial E_g/\partial V\|_T \ \partial V/\partial T\|_P$ (10^{-4} eV/°K)
G	L_{45}^-	-4.4	
	L_6^-	-4.6	
	L_6^-	-4.15	
	GAP		+1.8
	L_6^+	-5.95	
	L_{45}^+	-4.05	
	L_6^+	-5.5	

TABLE 14

$\underset{\sim}{k}$ index	$\underset{\sim}{k} = (k_x, k_y, k_z)$ (units of $2\pi/a$)	$\lvert\Delta \underset{\sim}{k}\rvert$ from L (units of $2\pi/a$)
k_1	(.434, .484, .476)	.072
k_2	(.432, .465, .464)	.085
k_3	(.402, .441, .454)	.123
k_4	(.422, .403, .471)	.128
k_5	(.458, .543, .5)	.06
k_6	(.487, .487, .56)	.0633

TABLE 15

Initial electronic state	Final electronic state	ξ from mode a coupling (eV)	ξ from mode b coupling (eV)
$\underset{\sim}{k}_1$	$\underset{\sim}{k}'_1$	1.95	1.03
$\underset{\sim}{k}_2$	$\underset{\sim}{k}'_2$	1.99	4.65
$\underset{\sim}{k}_1$	$\underset{\sim}{k}''_2$	0.9	1.26
$\underset{\sim}{k}_1$	$\underset{\sim}{k}'_3$	1.56	1.5
$\underset{\sim}{k}_4$	$\underset{\sim}{k}'_4$	0.45	2.18
$\underset{\sim}{k}_5$	$\underset{\sim}{k}'_5$	1.68	1.98
$\underset{\sim}{k}_6$	$\underset{\sim}{k}'_6$	0.53	1.06

TABLE 16

$\underset{\sim}{k}$ index	$\underset{\sim}{k} = (k_x, k_y, k_z)$ (units of $2\pi/a$)	$\lvert\Delta\underset{\sim}{k}\rvert$ from L (units of $2\pi/a$)
$\underset{\sim}{k}_1$	(.5029, .5029, .5029)	.005
$\underset{\sim}{k}_2$	(.5058, .5058, .5058)	.01
$\underset{\sim}{k}_3$	(.5115, .5115, .5115)	.02
$\underset{\sim}{k}_4$	(.5408, .5408, .5408)	.0707

TABLE 17

Initial electronic state	Final electronic state	ξ from mode a coupling (eV)	ξ from mode b coupling (eV)
$\underset{\sim}{k}_1$	$\underset{\sim}{k}'_1$	1.49	3.08
$\underset{\sim}{k}_2$	$\underset{\sim}{k}'_2$	0.278	1.4
$\underset{\sim}{k}_3$	$\underset{\sim}{k}'_3$	0.48	2.52
$\underset{\sim}{k}_4$	$\underset{\sim}{k}'_4$	0.57	1.34

FIGURE CAPTIONS

Fig. 1 Electronic energy band structure of SnTe.

Fig. 2 Electronic energy band structure of GeTe.

Fig. 3. Electronic energy band structure of PbTe.

Fig. 4 Imaginary part of the frequency dependent dielectric function $\epsilon_2(\omega)$ for SnTe.

Fig. 5 Imaginary part of the frequency dependent dielectric function $\epsilon_2(\omega)$ for GeTe.

Fig. 6. Imaginary part of the frequency dependent dielectric function $\epsilon_2(\omega)$ for PbTe.

Fig. 7 Energy bands near L in directions parallel to Λ and perpendicular to Λ at the L point for PbTe, $Sn_x Pb_{1-x}Te$ ($x = 0.25, 0.5$ 0.75) and SnTe.

Fig. 8 Two band perturbation result to illustrate the formation of the SnTe band edge structure.

(a) PbTe ordering

(b) Band crossing case assuming no interaction between the valence and conduction bands.

(c) Band crossing case assuming interaction between valence and conduction bands resulting in band edge structure similar to SnTe.

Fig. 9 Valence band energy contours in planes of constants k_z. (a) $k_z = 0$ corresponding to the hexagonal plane of the Brillouin zone, (b) $k_z = 0.04\ (2\pi/a)$, (c) $k_z = 0.08\ (2\pi/a)$. The energies are in eV with the zero energy reference defined to be at L point of the zone.

Fig. 10 Two views of Fermi surface pocket centered at L for SnTe. The hole Fermi energy is -0.11 eV (which corresponds to the -0.04eV contours in Fig. 9).

Fig. 11 Calculated and experimental temperature dependent energy gap $E_g(T)$ for PbTe. (The experimental data were from Ref. 31).

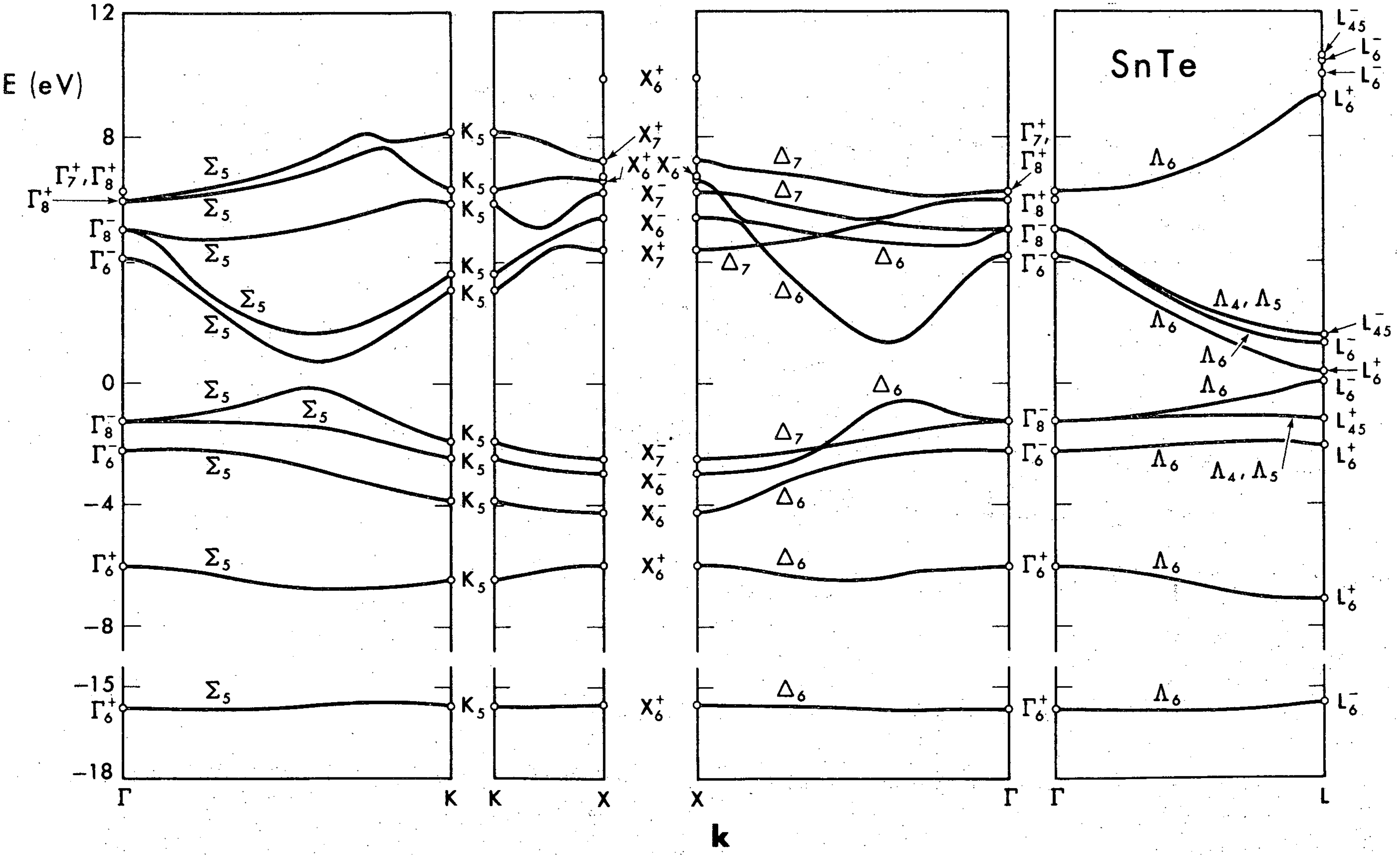
SnTe
E (eV)
12
8
0
−4
−8
−15
−18
Γ
K
K
X
X
Γ
Γ
L
k
Σ_5
Δ_6
Δ_7
Λ_6
Λ_4, Λ_5
K_5
Γ_7^+, Γ_8^+
Γ_8^+
Γ_8^-
Γ_6^-
Γ_6^+
X_6^+
X_7^+
$X_6^+ X_6^-$
X_7^-
X_6^-
L_{45}^-
L_6^-
L_6^+
L_{45}^+

Figure 1

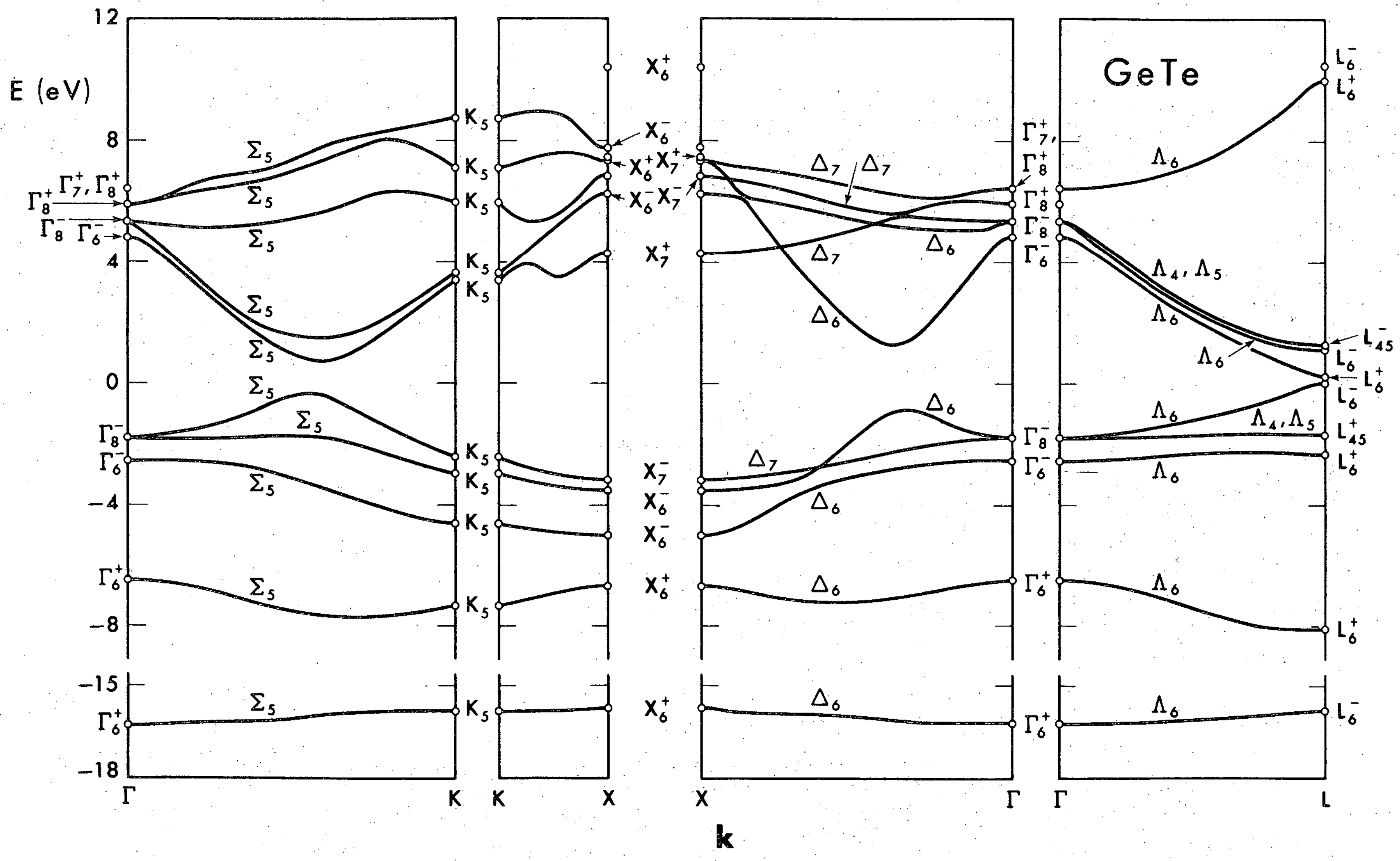
GeTe
E (eV)
12
8
4
0
−4
−8
−15
−18
Γ
K
K
X
X
Γ
Γ
L
k
Σ5
Δ7
Δ6
Λ6
Λ4, Λ5
K5
Γ7+, Γ8+
Γ8+
Γ8−
Γ6−
Γ6+
X6+
X6−
X7+
X7−
L6−
L6+
L45−
L45+

Figure 2

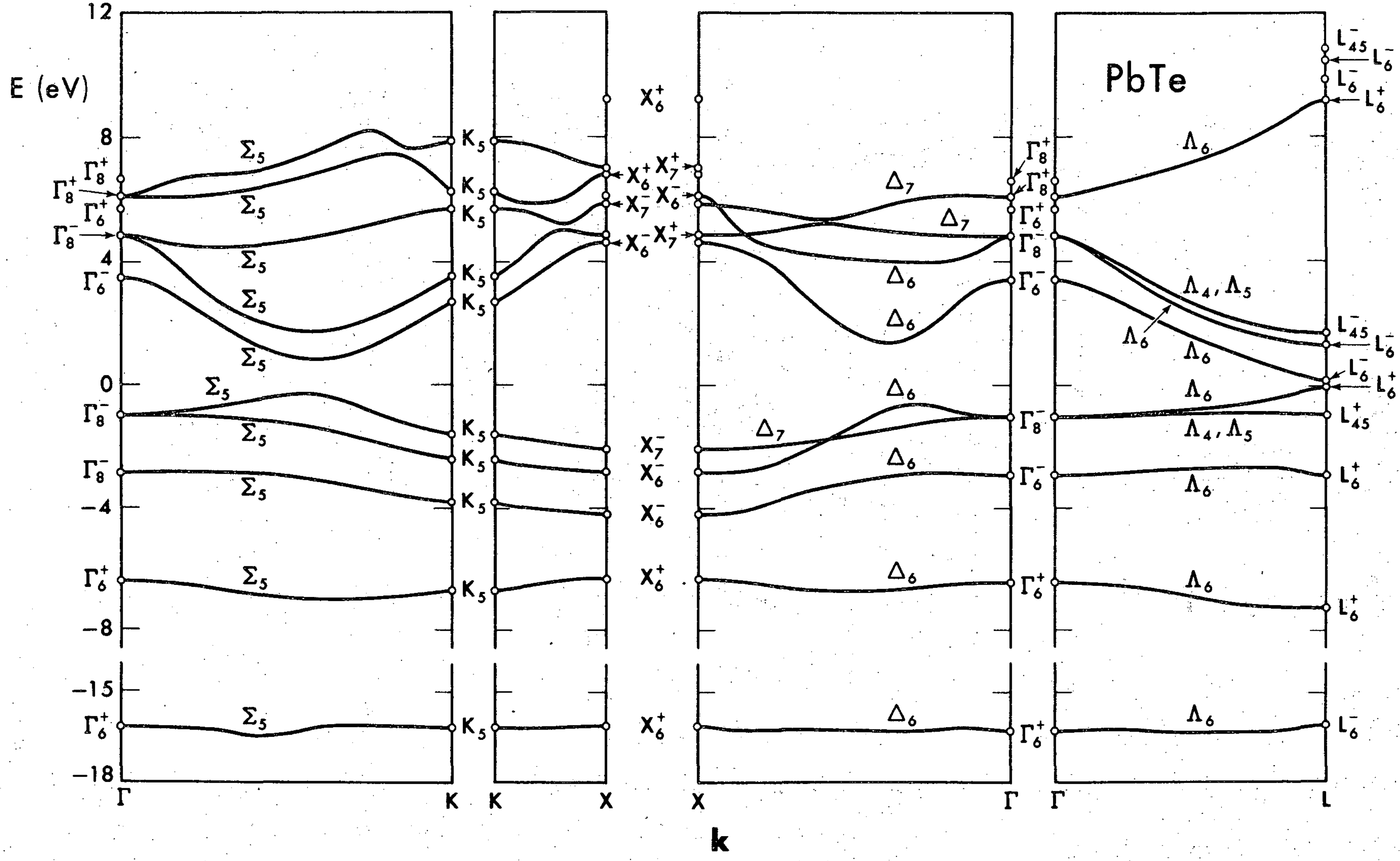
PbTe
E (eV)
12
8
4
0
−4
−8
−15
−18
Γ
K
K
X
X
Γ
Γ
L
k
Σ5
Δ6
Δ7
Λ6
Λ4, Λ5
K5
X6+
X7+
X6−
X7−
Γ8+
Γ6+
Γ8−
Γ6−
L45−
L6−
L6+
L45+

Figure 3

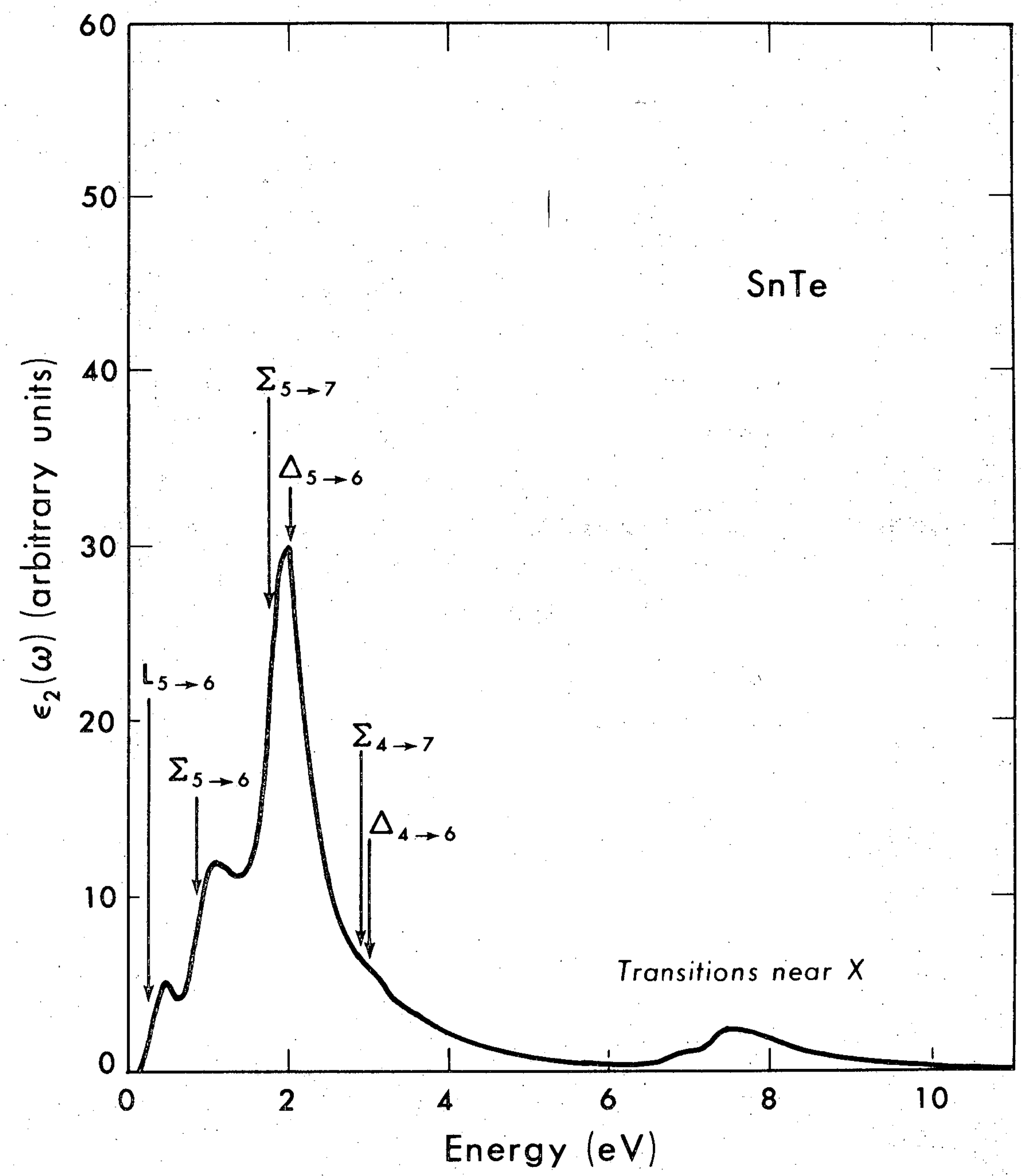
SnTe
$\epsilon_2(\omega)$ (arbitrary units)
Energy (eV)
$L_{5\rightarrow6}$
$\Sigma_{5\rightarrow6}$
$\Sigma_{5\rightarrow7}$
$\Delta_{5\rightarrow6}$
$\Sigma_{4\rightarrow7}$
$\Delta_{4\rightarrow6}$
Transitions near X
0
10
20
30
40
50
60
0
2
4
6
8
10

Figure 4

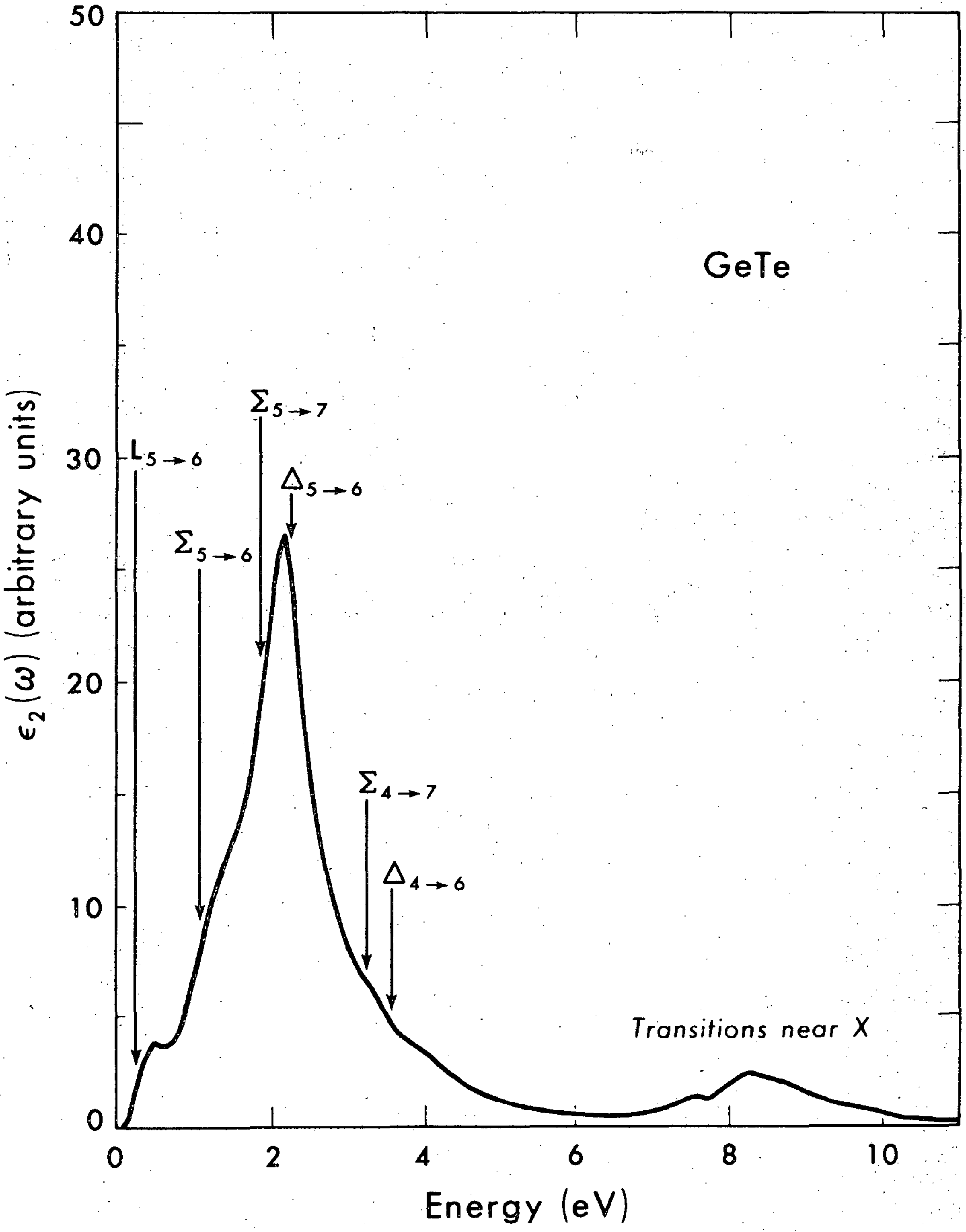
GeTe
$\epsilon_2(\omega)$ (arbitrary units)
Energy (eV)
$L_{5\to6}$
$\Sigma_{5\to6}$
$\Sigma_{5\to7}$
$\Delta_{5\to6}$
$\Sigma_{4\to7}$
$\Delta_{4\to6}$
Transitions near X
0
10
20
30
40
50
0
2
4
6
8
10

Figure 5

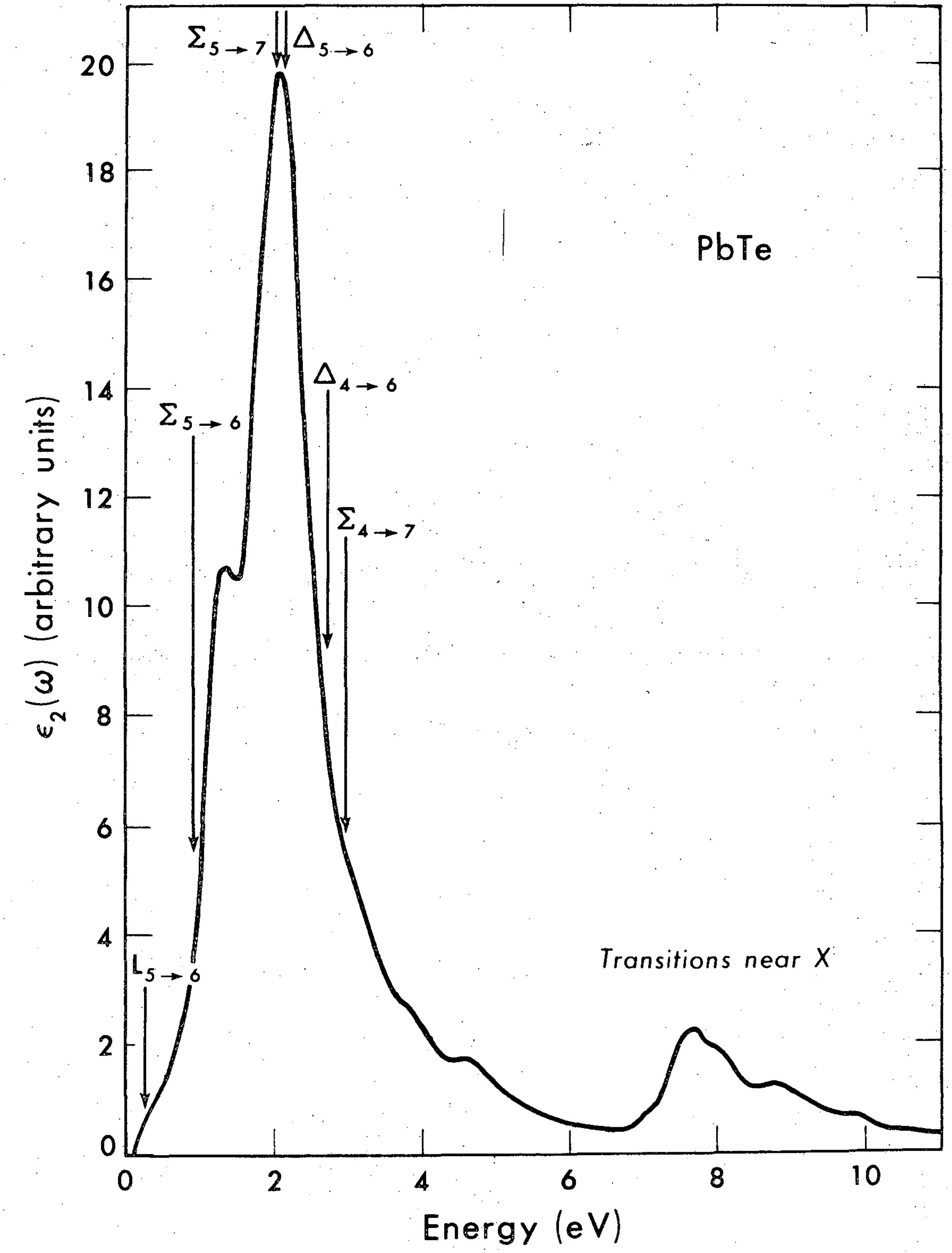
$\Sigma_{5\to7}$
$\Delta_{5\to6}$
PbTe
$\Delta_{4\to6}$
$\Sigma_{5\to6}$
$\Sigma_{4\to7}$
$L_{5\to6}$
Transitions near X
$\epsilon_2(\omega)$ (arbitrary units)
Energy (eV)
0
2
4
6
8
10
12
14
16
18
20

Figure 6

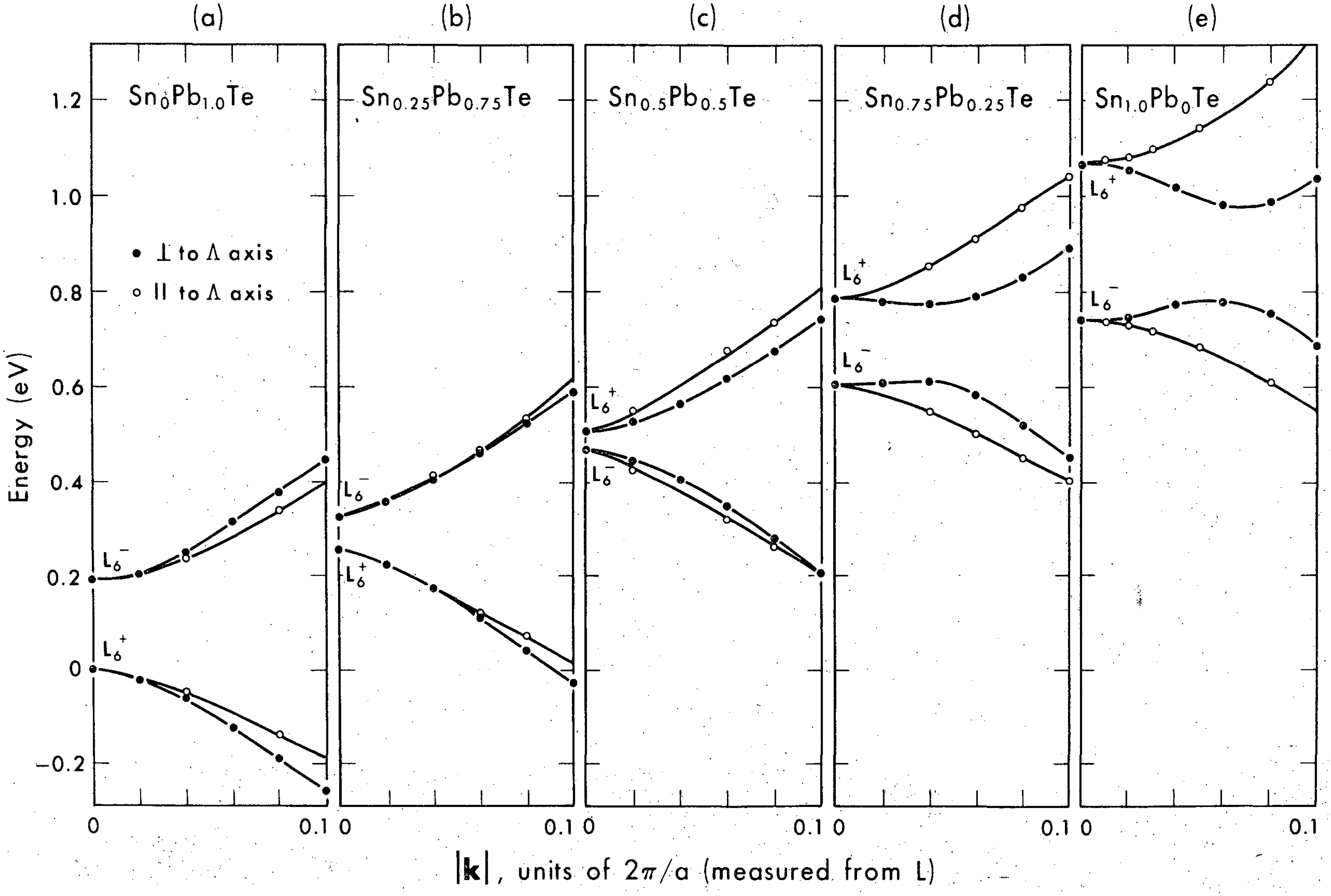
(a)
(b)
(c)
(d)
(e)
Sn$_0$Pb$_{1.0}$Te
Sn$_{0.25}$Pb$_{0.75}$Te
Sn$_{0.5}$Pb$_{0.5}$Te
Sn$_{0.75}$Pb$_{0.25}$Te
Sn$_{1.0}$Pb$_0$Te
● ⊥ to Λ axis
○ ‖ to Λ axis
L_6^-
L_6^+
Energy (eV)
1.2
1.0
0.8
0.6
0.4
0.2
0
−0.2
0
0.1
$|\mathbf{k}|$, units of $2\pi/a$ (measured from L)

Figure 7

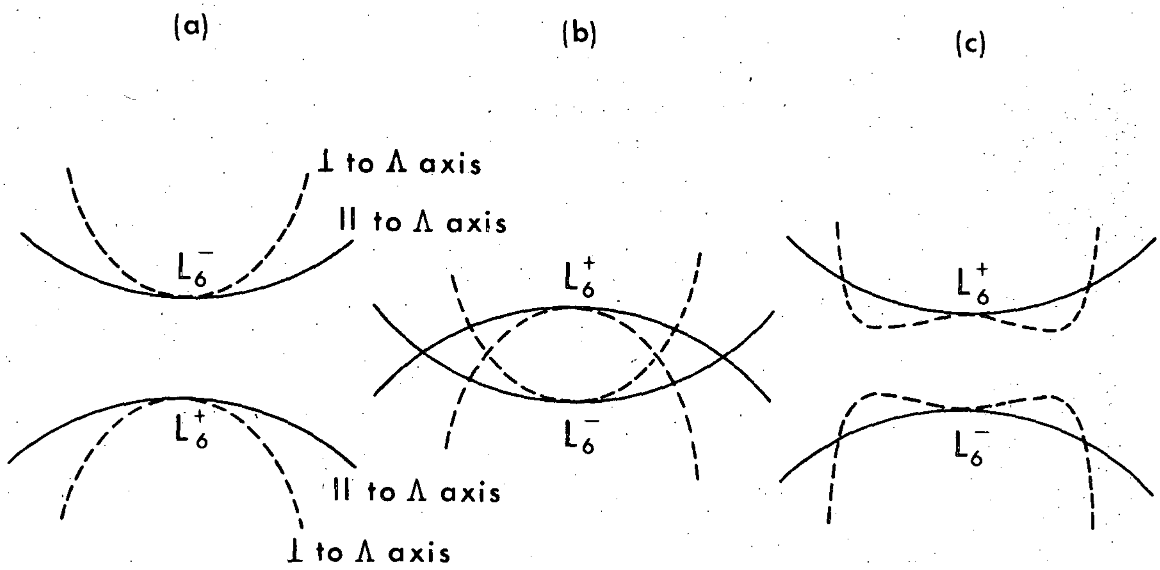

Figure 8

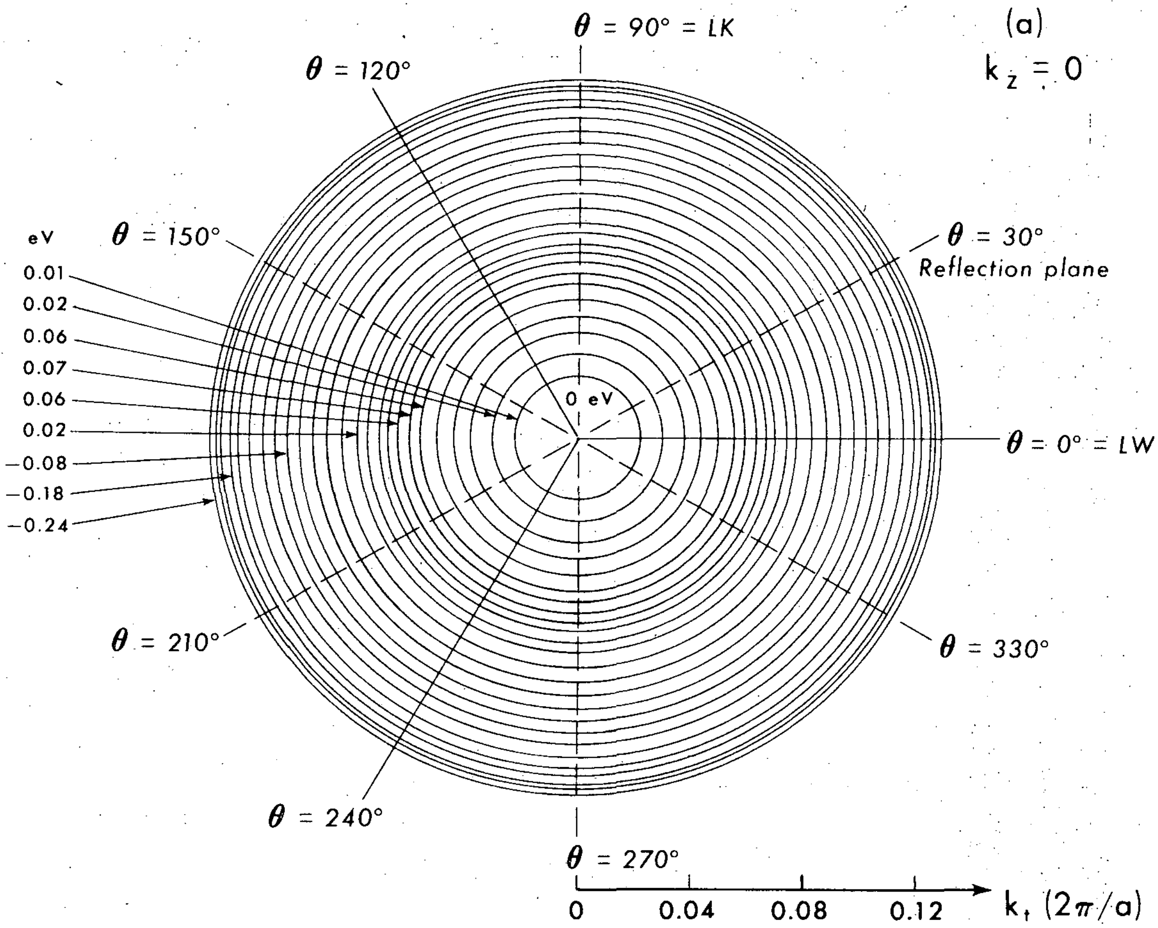
(a)
$k_z = 0$
θ = 90° = LK
θ = 120°
θ = 150°
θ = 30°
Reflection plane
θ = 0° = LW
θ = 210°
θ = 330°
θ = 240°
θ = 270°
0 eV
eV
0.01
0.02
0.06
0.07
0.06
0.02
−0.08
−0.18
−0.24
0
0.04
0.08
0.12
k_t $(2\pi/a)$

Figure 9a

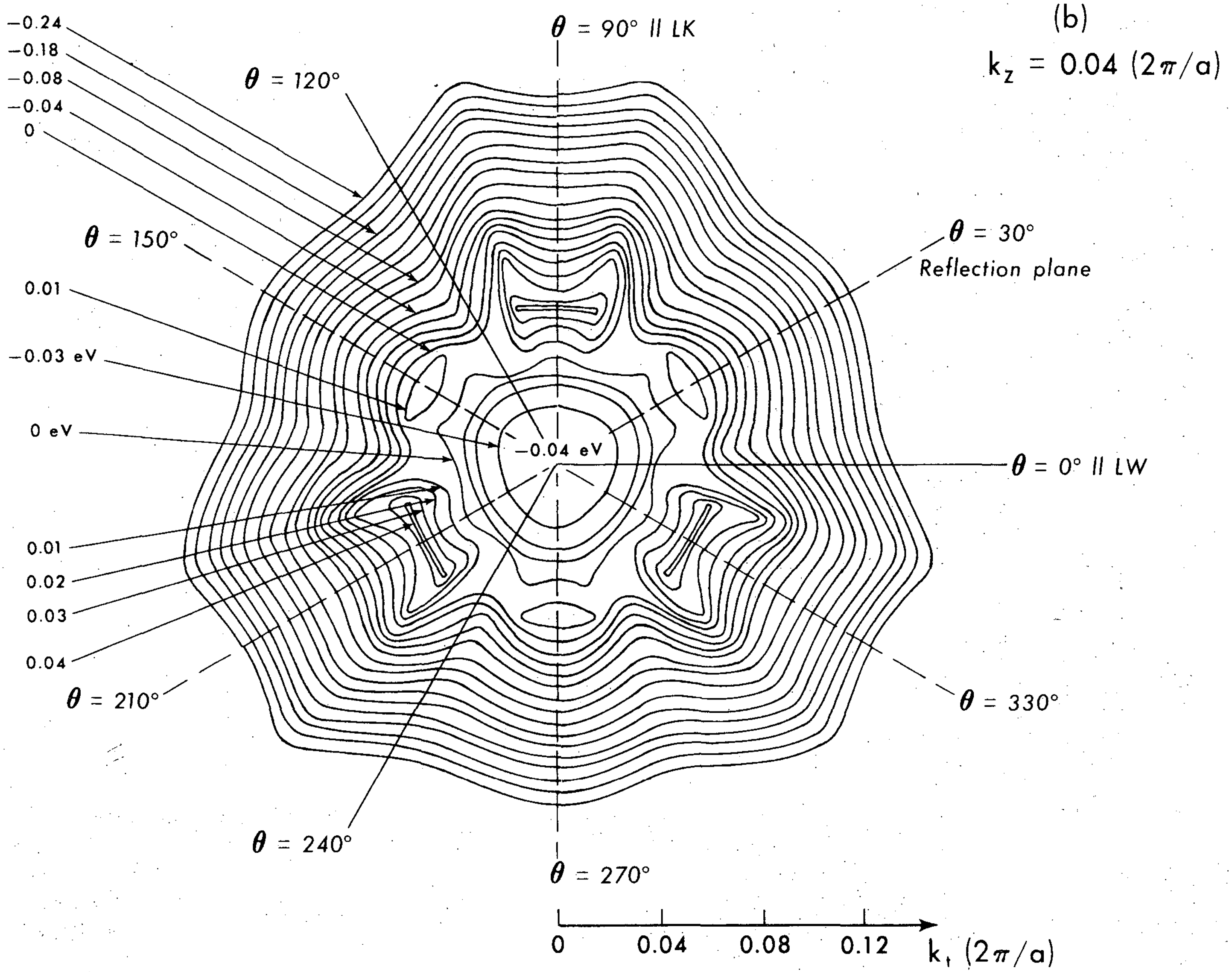
(b)
$k_z = 0.04\ (2\pi/a)$
θ = 90° ‖ LK
θ = 120°
θ = 150°
θ = 30°
Reflection plane
θ = 0° ‖ LW
θ = 210°
θ = 240°
θ = 270°
θ = 330°
−0.24
−0.18
−0.08
−0.04
0
0.01
−0.03 eV
0 eV
−0.04 eV
0.01
0.02
0.03
0.04
0
0.04
0.08
0.12
$k_t\ (2\pi/a)$

Figure 9b

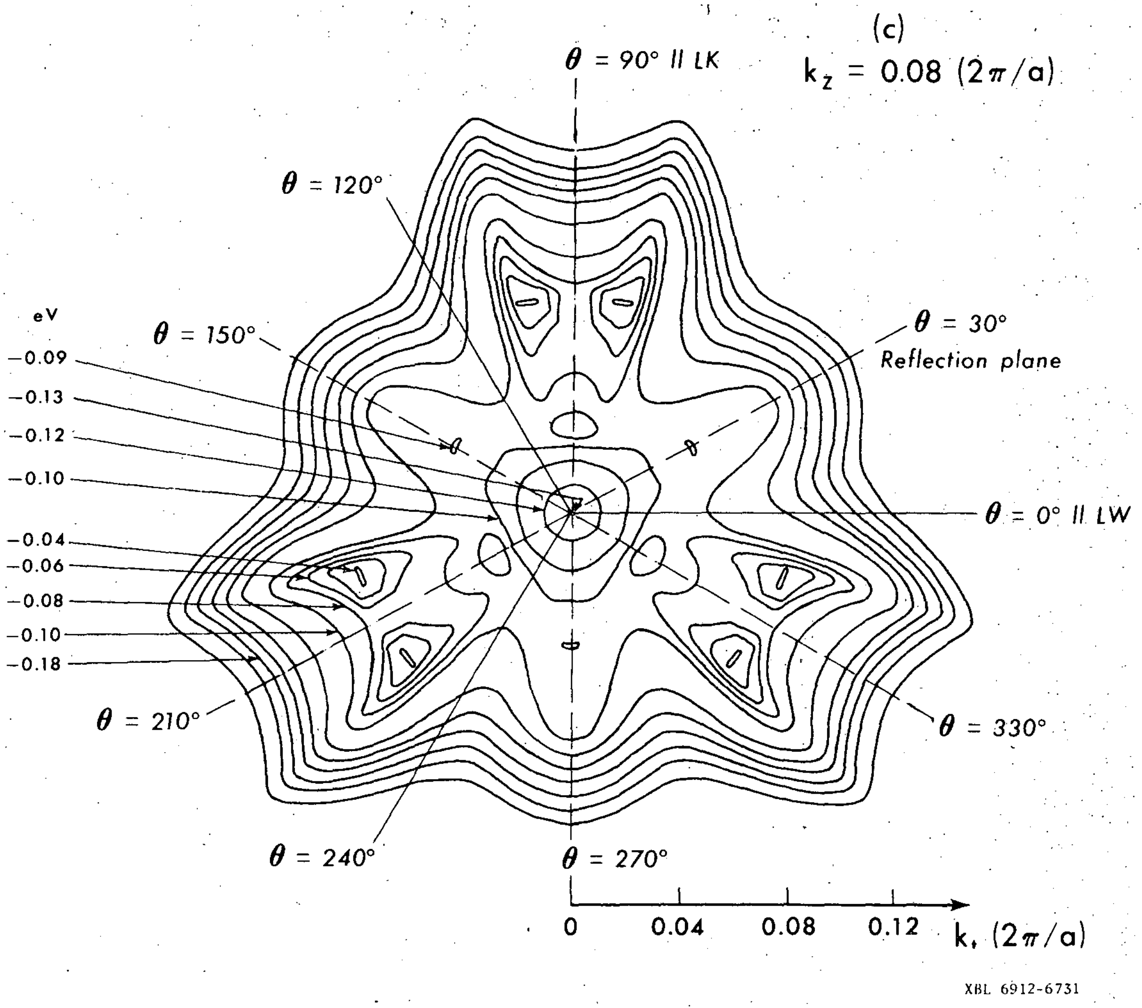
(c)
k_z = 0.08 (2π/a)
θ = 90° ∥ LK
θ = 120°
θ = 150°
θ = 30°
Reflection plane
θ = 0° ∥ LW
θ = 210°
θ = 240°
θ = 270°
θ = 330°
eV
−0.09
−0.13
−0.12
−0.10
−0.04
−0.06
−0.08
−0.10
−0.18
0
0.04
0.08
0.12
k₊ (2π/a)
XBL 6912-6731

Figure 9c

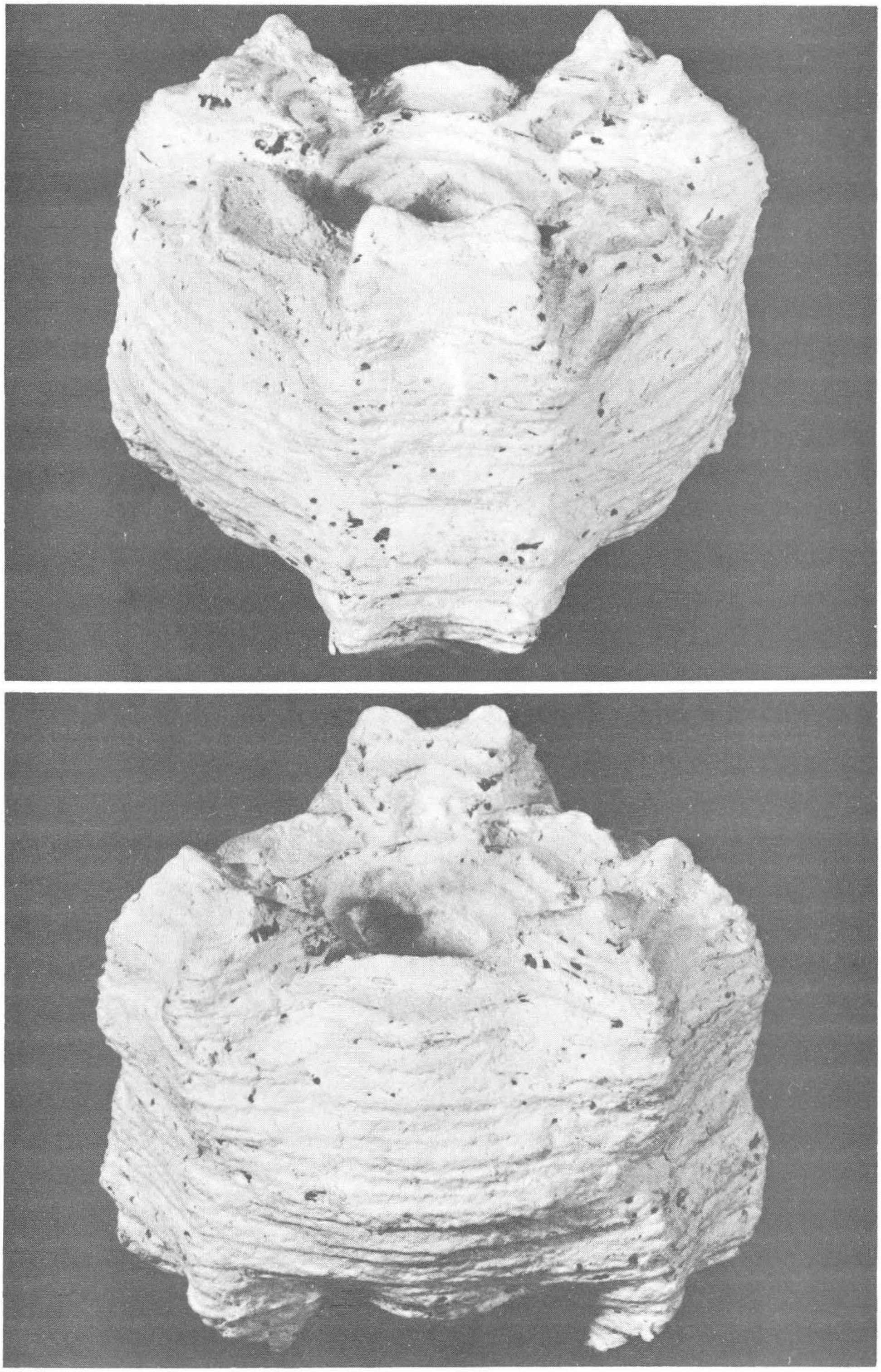

XBB 702-637

Figure 10

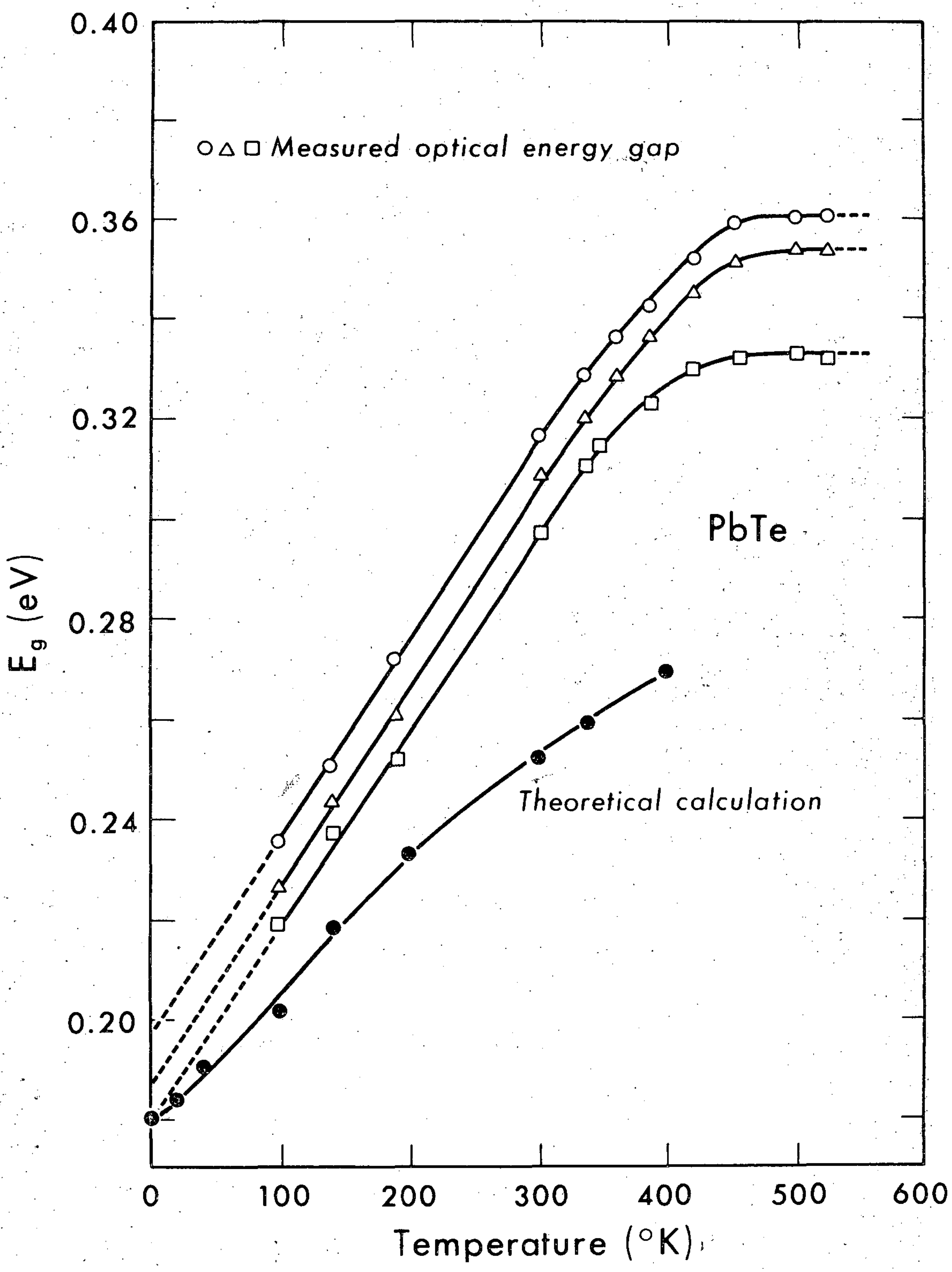
○△□ Measured optical energy gap
PbTe
Theoretical calculation
0.40
0.36
0.32
0.28
0.24
0.20
E_g (eV)
0
100
200
300
400
500
600
Temperature (°K)

Figure 11

TECHNICAL INFORMATION DIVISION
LAWRENCE RADIATION LABORATORY
UNIVERSITY OF CALIFORNIA
BERKELEY, CALIFORNIA 94720